Photometric Studies for Color Magnitude Diagram and Mass Distribution of Globular Clusters

P. Choochalerm[1*] and S. Wannawichian[1,2]

[1]Department of physics and Materials Science, Faculty of Science, Chiang Mai University, Chiang Mai, Thailand

[2]National Astronomical Research Institute of Thailand (NARIT), Chiang Mai, Thailand

*E -mail: paksapak@gmail.com

Abstract

We present BV Photometry for the globular clusters (GCs) M3 (NGC 5272), M92 (NGC 6341) and M107 (NGC 6171), which are analyzed by Aperture Photometry Tool (APT). The optical images of M3 were taken by 2.4m Telescope and the images of M92 and M107 were taken by 0.5m Telescope at Thai National Observatory in Chiang Mai, Thailand. The magnitudes of stars in three globular clusters were determined. Furthermore, the luminosity of each star was converted based on its BV magnitude, which accordingly relates to color-magnitude diagram (CMD). CMD can describe range of Turn-off point and ages of cluster. In addition, we also use mass-luminosity relation for create mass distribution of three GCs. In this study, CMD of above clusters were analyzed and compared with the result from previous studies by Buonanno, et al. (1994) [1], Stetson and Harris (1988) [2] and Ferraro, et al. (1991) [3]. The similar evolution was shown in CMD, although our studies have less points of data. In addition, we used mass-luminosity relation to create mass distribution of three GCs. For M3, M92 and M107 we found that most of stars have mass ranges between 4.0-4.9 solar mass, 0.98-1.59 solar mass and 1.34-1.97 solar mass respectively.

Keywords: Globular cluster, Color magnitude diagram, Mass distribution

Introduction

The globular cluster (GC) is one of many objects in the universe that scatters all around us. The globular cluster is a group of many stars which bound into each other with strong gravity [4]. As a result, they have high density at the center. Every star in a globular cluster forms and evolves to the end of their lifetime at the same time. Therefore we can expect that their physical properties should be similar.

Hertzsprung-Russell diagram or HR-diagram [4], which is the relation plot between stellar magnitudes and spectral types, is used to describe the properties of globular cluster. It is one essential tool for classifying stellar types including their properties.

For this study, Aperture Photometry Tool or APT, which is a photometric freeware, was selected for data analysis. Combined images of each GC were used in photometric method. We analyzed and calculated luminosity from apparent magnitude. We used Color Magnitude Diagram or CMD, which is variant of HR-diagram and used to describe the properties of GCs. The results are plots of color index [5] or B-V and apparent magnitude. Different shapes of graph for each GC were presented. Furthermore, we study mass distribution for each GC. The mass-luminosity relation [6] was used to find mass from stellar brightness. The most populated mass range of each GC will be presented.

Materials and Methods

Instruments and observations

All images in this research were taken at Thailand National Observatory (TNO) at Inthanon mountain, Chiang Mai, Thailand, latitude 18°34'N, longitude 98° 28'E and altitude 2,457 meters above sea level. The Instruments are 2.4-meter reflecting telescope and 0.5-meter Schmidt-Cassegrain Robotic Telescope that were controlled by National Astronomical Research Institute of Thailand (NARIT).

M3 was taken by 2.4-meter reflecting telescope on February 17th, 2016, in Figure 1. All images were taken in B and V filters by 4k camera and the exposure time for each image is 60 seconds. The CCD temperature is -110 °c.

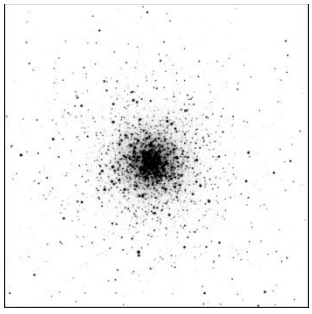

Figure 1 Image of M3 (NGC5272) was taken by 2.4-meter reflecting telescope at TNO.

M92 and M107 were taken by 0.5-meter Schmidt-Cassegrain Robotic Telescope with the exposure time 30 seconds. The instrument, which uses Andor Technology, operates with 2.4-meter reflecting telescope. The CCD temperature is -65 °c. All images were taken in B and V filters.

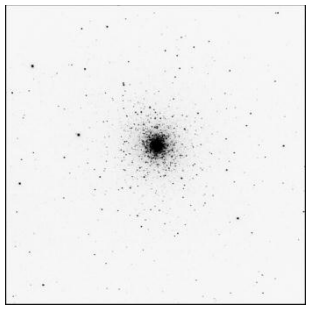

Figure 2 Image of M92 (NGC6241) was taken by observation by 0.5-meter Schmidt-Cassegrain Robotic Telescope at TNO.

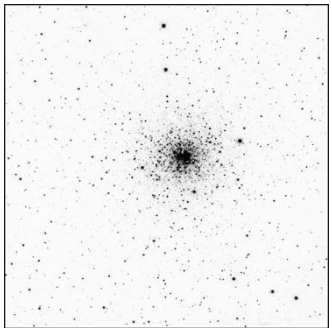

Figure 3 Image of M107 (NGC6171) was taken by 0.5-meter Schmidt-Cassegrain Robotic Telescope at TNO.

Analysis of the stellar brightness by APT

Aperture Photometry Tool (APT) was used to determine the magnitudes of stars in GCs. The analyzed data contains the information about positions and instrumental magnitudes of stars.

Creation of Color Magnitude Diagram and Mass Distribution

The calibration of instrument can be done by referring to real magnitude of standard star from SIMBAD Astronomical Database (http://gclusters.altervista.org/).

Next, the magnitude was converted to luminosity by using color extinction E(B-V) from a Galactic Globular Clusters Database (http://gclusters.altervista.org/).

Converting Magnitude to Luminosity

From the apparent magnitude of an object from APT, the luminosity [4] is one of the properties that can define other physical parameters, for example mass, radius, temperature etc. For this study, the procedures are following.

Visible absolute magnitude was calculated from distance modulus, m-M, which is referred to a galactic globular database. Next, we converted V absolute magnitude to luminosity in solar luminosity by [4]

$$M_* - M_{sun} = -2.5 log \frac{L_*}{L_{sun}} \quad (1)$$

M_* is an object absolute magnitude. M_{sun} is the solar absolute magnitude. L_* is an object's luminosity and L_{sun} is the solar luminosity.

We obtained luminosity for B magnitude from the luminosity in the V filter by following equation [4]

$$B - V = -2.5 log \frac{L_B}{L_V} \quad (2)$$

B and V are apparent magnitudes in B and V filters respectively. L_B and L_V are luminosities in B and V filters.

Finally, color magnitude diagram (CMD) was created by using analytical data from APT.

The method of creating mass distribution

Mass-luminosity relation [6] was used for creating mass distribution of globular clusters. The relation is defined as [6]

$$L \propto Mass^{3.5} \quad (3)$$

After the masses of stars were converted from luminosity, the consequence steps are: mass ranges were determined in different star systems. Number of stars was count for each mass range.

Center value for each mass range and number of stars was plotted to present the mass distribution for each cluster.

Results and Discussion

Color Magnitude Diagram and Mass Distribution of M3 (NGC5272)

CMD of M3 from this study is presented in Figure 4. Our result is compared to previous study by Buonanno et al. (1994) [1] (Figure 5). We found that our result has less data than previous study and most of data locates in the upper region of main-sequence. In the other hand, data of stars which have V>18.7 cannot be detected. However, morphology of star evolution in this work is still similar to previous work. Most of population of stars in this work are giant or red giant stars.

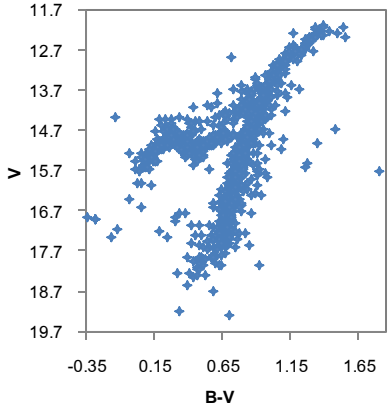

Figure 4 CMD of M3 (NGC5272) from this study. Color extinction (E(B-V)) was considered for color index (B-V) in horizontal axis.

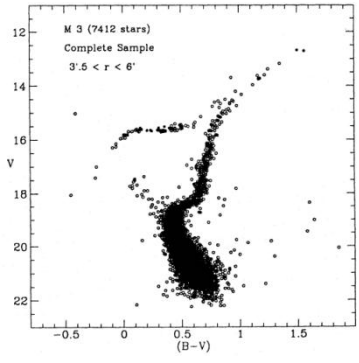

Figure 5 CMD of M3 (NGC5272) from Buonanno et al. (1994) [1]

In Figure 6, the histogram of mass distribution was shown. The most stars in M3 have 4.0-4.9 solar mass.

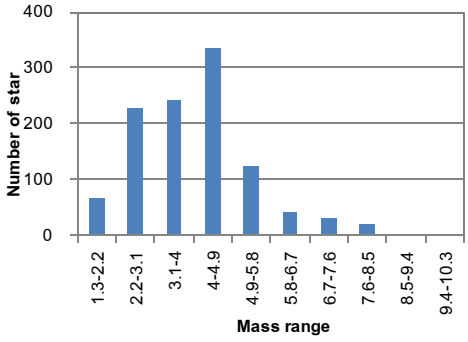

Figure 6 Mass distribution histogram of M3 (NGC5272)

After histogram was created, center value for each mass range is determined in Figure 7 to present the characteristics of mass distribution. We found that most stars have 4.45 solar mass.

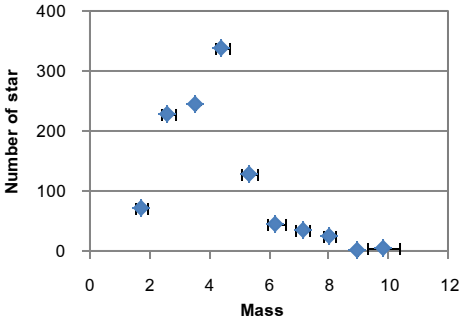

Figure 7 Mass distribution graph of M3 (NGC5272)

Color Magnitude Diagram and Mass Distribution of M92 (NGC6341)

CMD for M92 is shown in Figure 8 to compare with previous study by Stetson and Harris (1988) [2] (Figure 9). The similar morphology diagram is shown for comparison with less data for our result. CMD showed that most of stars in M92 are giant or red-giant.

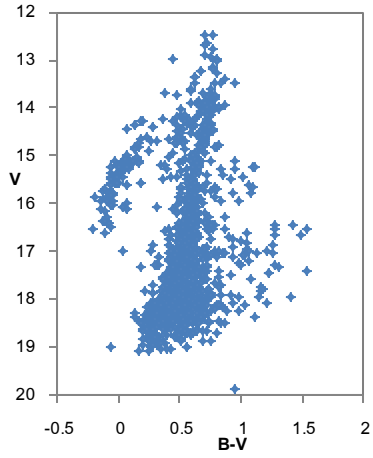

Figure 8 CMD of M92 (NGC6341) from this study. Color extinction (E(B-V)) was considered for color index (B-V) in horizontal axis.

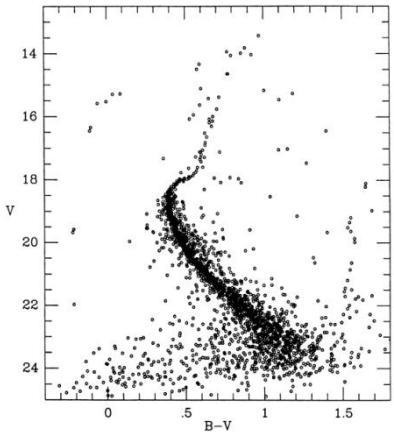

Figure 9 CMD of M92 (NGC6341) from previous study by Stetson and Harris (1988) [2]

Figure 10 shows mass distribution of M92 where most of stars are in 0.98-1.59 mass range (in solar mass).

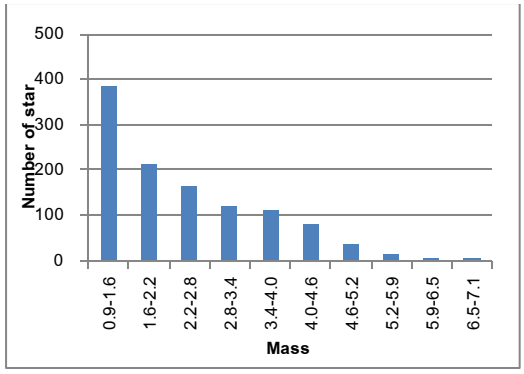

Figure 10 Mass distribution histogram of M92 (NGC6341)

Mass distribution for center value of each mass range is shown in Figure 11. We found that most population have 1.285 solar mass.

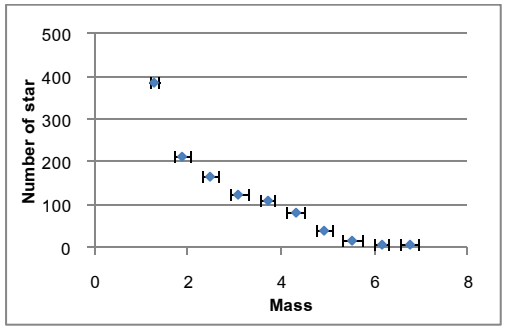

Figure 11 Mass distribution graph of M92 (NGC6341)

Color Magnitude Diagram and Mass Distribution of M107 (NGC6171)

Figure 12 shows CMD of M107 from this study. According to CMD from previous study by Feraro et al. (1991) [3] (Figure 13), there are two groups of stars (faint and bright stars). However we found that are mostly bright stars (V<19), which were detected by APT for this work. However, the trend of star evolution of M107 is similar to previous study. As same as M3 and M92, most stars in M107 are giants and red-giants

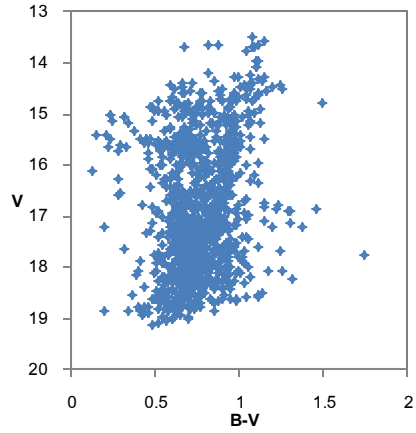

Figure 12 CMD of M107 (NGC6171) from this study. Color extinction (E(B-V)) was considered for color index (B-V) in horizontal axis.

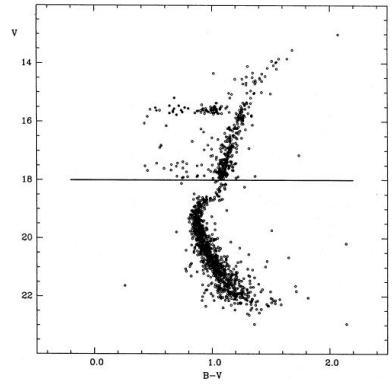

Figure 13 CMD of M107 (NGC6171) from previous study by Feraro et al. [3] (1991). A straight line has been drawn on the plot to divide the bright and faint samples.

In Figure 14 below, mass distribution shows that most stars have 1.34-1.97 solar mass.

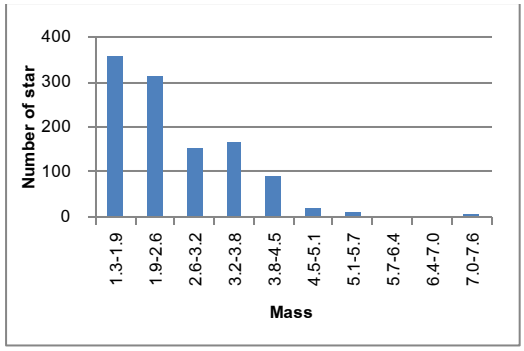

Figure 14 Mass distribution histogram of M107 (NGC6171)

From mass distribution from Figure 15, we found that most stars have 1.655 solar mass.

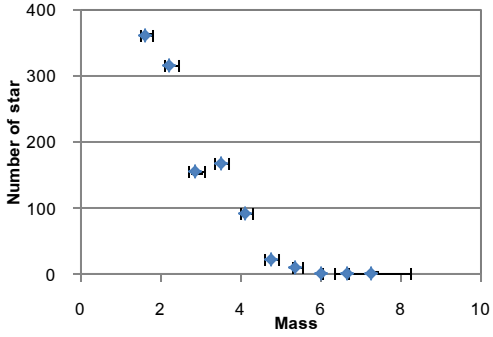

Figure 15 Mass distribution of M107 (NGC6171)

Conclusions

We obtained B and V photometry for M3, M92 and M107. There are two main results from this study. One of them is Color Magnitude Diagram (CMD) for each globular cluster. The other result is their mass distributions.

For summary, CMDs mostly shows bright stars. The evolution stage in which most stars were detected is above main-sequence. Thus, these CMDs trends imply that the stars in our study are in giant state of their life time. In addition, the mass-luminosity relation is used for creation mass distribution of stars that we detected for each globular cluster. The results are following:

1. For M3, M92 and M107, most of population are in mass ranges 4.0-4.9 solar mass, 0.98-1.59 solar mass and 1.34-1.97 solar mass respectively.

2. Center value for each range was considered. There are 4.45 solar mass for M3, 1.285 solar mass for M92 and 1.655 solar mass for M107.

For remark: the mass distribution showed only data for some stars, which are detected by APT.

Acknowledgments

We would like to thank additional advice from Mr. Somsawat Rattanasoon. All images are under our collaboration with National Astronomical Research Institute of Thailand (NARIT).

References

[1] Buonanno R., *et al.* 1994. "The stellar population of the globular cluster M3 I. Photographic photometry of 10,000 stars". **Astron. Astrophys journal**. 290, 69-103.

[2] Stetson, P.B. and Harris, W.E. 1988. "CCD Photometry of the Globular cluster M92". **The Astronomical journal**, 96(3):909-1161.

[3] Ferraro, F.R. *et al.* 1991. "CCD-Photometry of galactic globular clusters-III. NGC6171". **Mon. Not. R. astr**. 252:357-377.

[4] Carroll, B. W. and Ostlie, D. A. (2007). An Introduction to Modern Astrophysics. Boston, U.S.: Pearson Addison-Wesley.

[5] Freedman R., Kaufman W. 2002. **Universe: (6th)**. New York, U.S.:W.H. Freeman and Company.

[6] Padmanabhan T. 2001. **"Theoretical Astro-physics Volume II: Stars and Stellar Systems"**. Cambridge, U.K.: Cambridge university press.

Variability Study of Active Galactic Nuclei at Visible and X-ray Wavelength

T. Thongmeearkom[1], P. Surarittikul[1*], M. Schramm[2] and W. Rujopakarn[3,1]

[1] Department of Physics, Faculty of Science, Chulalongkorn University, 254 Phayathai Road, Patumwan, 10330, Thailand

[2] National Astronomical Observatory of Japan, 2-21-1 Osawa, Mitaka, Tokyo 181-8588, Japan

[3] Kavli IPMU, University of Tokyo, 5-1-5 Kashiwanoha, Kashiwa, Chiba Prefecture 277-8583, Japan

E-mail: pakawee.stk@gmail.com

Abstract

We study short-term variability of active galactic nuclei (AGNs) at visible and X-ray wavelength by conducting photometric monitoring method; these samples are selected from 330 quasars at redshift $z < 0.3$ in the Hamburg/ESO Catalog. We obtain data at visible wavelength in Johnson B, V and R filters with Thai Robotic Southern Hemisphere Telescope at Cerro Tololo Inter-American Observatory, Chile, and at X-ray in 2.0 – 20.0 keV band from the Monitor of All-Sky X-ray Image (MAXI) on board the International Space Station. We construct light curves of each AGN in magnitude-time for visible light data and in flux-time for X-ray using python-based algorithms created by Vijarnwannaluk et al. [3]. Our goal is searching for variability at visible and X-ray wavelength to identify potential targets for reverberation mapping follow-up. Here we present early results from the study that indicates marginal variability in X-ray and visible wavelength.

Keywords: Active galactic nuclei, MAXI, Photometric monitoring, Reverberation mapping

Introduction

Active galactic nuclei (AGNs) are regions at the center of galaxies which show variability in brightness at all wavelength of electromagnetic waves. This variability results from high energy release from accreting supermassive black hole (SMBH) as dense mass in the accretion disk falling into the black hole, which is a potential to study structure of the AGNs. We study the AGNs' structure by observing their spectrum known as reverberation mapping technique. However, the reverberation mapping take a lot of observation time, thus we use the other way: photometric monitoring which observes flux intensity of AGNs at a period of time. If an object is found the outburst, it has a potential to study the reverberation mapping afterwards. If we find the outburst in many wavelengths, it means that object has more potential.

In this study, our main objective is to monitor large number of AGNs to find the outburst at visible light and X-ray wavelength by using Thailand's 0.6-m robotic telescope for visible light data and Monitor of All-sky Image (MAXI) for X-ray and observe pattern of two data.

Materials and Methods

The Sample

As recommended by Schulze et al. [1] and Wisotzki et al. [4], We selected samples of well-defined quasars from the Hamburg/ESO catalog (HES) the wide-angle surveys of quasars mainly in the southern hemisphere conducted by 1-m Schmidt telescope with its 4-degree prism in La Silla Observatory, Chile. The survey consists of 380 fields covering 9000 deg^2 containing quasars with

magnitude between 13 and 18 ($13 < B_j < 18$) and redshifts ranging from $z = 0$ to 3 with majority between $0 < z < 1$. In this study we are interested in bright quasars with $B_j < 18$ and redshifts lower than 0.3 ($z < 0.3$) which covers approximately 330 objects in the catalog.

To calculate the magnitude of AGNs at visible light, we use data of reference stars from The Fourth US Naval Observatory CCD Astrograph Catalog (UCAC4) containing stars of magnitude 8 to 16.

Visible Light Photometry

We obtain visible light data from Thai Southern Hemisphere Telescope, a PROMPT 0.6-meter robotic Ritchey-Chrétien telescope managed by University of North Carolina which each picture taken covers an area of 22.6 x 22.6 arcmin^2. We submit jobs and download data on Skynet website, and conduct four algorithms used in Vijarnwannaluk et al. [3] to analyze short-term variability and plot into magnitude-time graph, following these steps:

The first algorithm separates images into Johnson B, V, and R filters, combines images taken in the same day using SWARP and extracts data of each object using SExtractor. Since individual object does not appear in the same position in every image, SWARP will align the object before the combination. As the fluxes of constant stars should not change much over time, the algorithm selects the reference stars which show little flux ratio difference compared to the others, and produces a text file containing a list of stars with their right ascension, declination and magnitudes.

Next, the second algorithm checks quality of the AGN whether it appears in the image; the position of the AGN in each image must not differ more than 10 arc seconds, and shows signal-to-noise ratio more than defined value (flux/flux error > 12).

After that, the third algorithm calculates the zero point magnitude in each day using data from UCAC4. The reference stars must appear in all images with the magnitude lower than 18, have the flux more than twice of the AGN, be out from the AGN more than 3 arc seconds, portray ellipticity less than 0.3, and show position difference between the catalog and the extracted file less than 10 arc seconds. Then we use a sigma clip method to discard any outlier stars. Finally, the data of remaining stars will be exported as a text file.

The fourth algorithm calculates the magnitude of the AGN by comparing the AGN's flux to the zero point using flux scaling method with the magnitude of the zero point typically from UCAC4. It also finds error by using error from SExtractor and error when calibrate magnitude then use the propagation of error to calculate the final error. The program then exports a text file containing data of magnitude with respect to modified Julian date. Finally, we plot the light curve of individual AGN to see if the outburst is occurred.

X-ray Photometry

As recommended by Ueno et al. [2], we obtain X-ray data from the Monitor of All-Sky X-ray Image (MAXI) board the International Space Station which monitors the X-ray variability of all sky objects every 96 minutes. There are two types of detectors in MAXI: Gas Slit Camera (GSC) which consists of 12 gas proportional counters covering band of 2-30 keV and Solid-state Slit Camera (SSC) covering 0.5–10 keV band.

Unlike optical, the X-ray data from MAXI already contains a final light curve for each individual target position; hence we can plot data directly from the text file. In this study we conduct data in 2.0-20.0 keV. Then, we manually cut off some data with high error bar and apply python-based algorithm to plot the light curve from the text file with flux photon/cm^2/second in vertical axis and modified Julian date in horizontal.

Results and Discussion

We have monitored samples of 30 objects with using our algorithms. From the analysis, 6 objects show good variability which is approximately 20% of the samples. To demonstrate, we present light curves of HE0345+0056, HE1348-1758, HE 1349-1834, HE1417-0909 and HE1519-0634 in Johnson B, V, R

and X-ray in 2.0-20.0 keV band generated by MAXI in comparison.

Short-term Variability of HE0345+0056

HE0345+0056 has B_j = 14.87 with redshift 0.029. The data covers around 239 observing nights with an average cadence of 2.234 days.

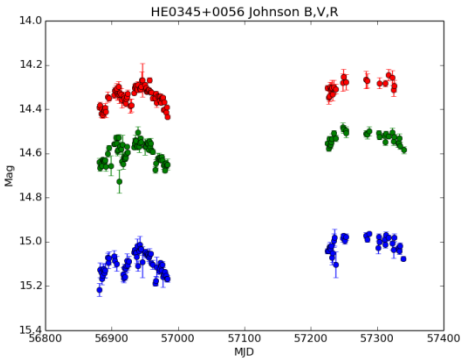

Figure 1 Variability of HE0345+0056 in Johnson B, V, and R filters

In Figure 1, variability of HE0345+0056 in Johnson B, V, R is clearly seen. The graph shows two significant peaks of about 0.2 magnitude at MJD 56900 and MJD 56940 respectively, and another peak of 0.1 magnitude at around MJD 56980.

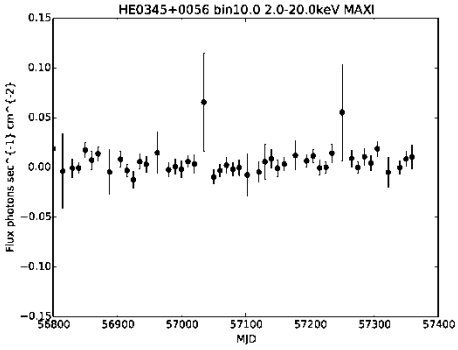

Figure 2 Variability of HE0345+0056 at X-ray in 2.0-20.0 keV band

As shown in Figure 2, variability at X-ray fluctuates throughout the observation time and some data shows large error bars. During MJD 56900-56950, the light curve shows the same M-shaped pattern comparing to the one in Johnson B, V, R but not as clearly as the optical one.

Short-term Variability of HE1348-1758

HE1348-1758 has B_j = 15.77 with redshift 0.014. The data covers around 421 observing nights with average cadence of 1.508 days.

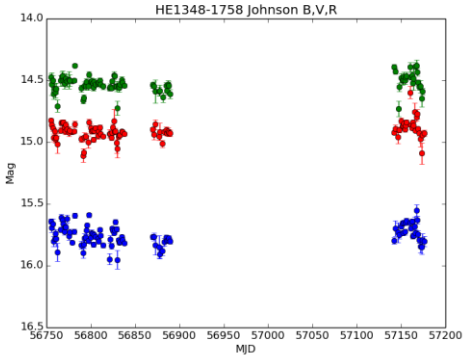

Figure 3 Variability of HE1348-1758 in Johnson B, V, and R filters

In Figure 3, variability of HE1348-1758 in Johnson B, V, R is fluctuated during MJD 56750-56900, yet shows a significant peak of about 0.3 magnitude between MJD 57150-57200

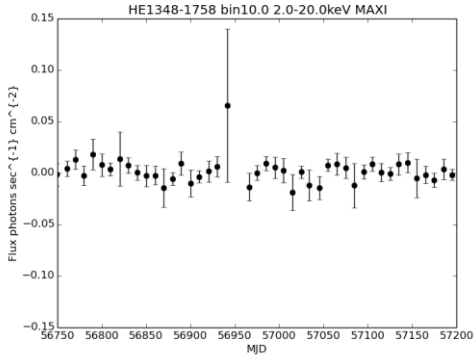

Figure 4 Variability of HE1348-1758 at X-ray in 2.0-20.0 keV band

As shown in Figure 4, variability at X-ray fluctuates throughout the observation time and shows no significant signs of outburst: no exact increase is found around MJD 57150 like the optical one. Despite there is a data point with high value around MJD 56950, it comes up with large error bar thus it cannot be confirmed as a sign of outburst.

Short-term Variability of HE1349-1834

HE1349-1834 has B_j = 16.9 with redshift 0.185. The data covers around 156 observing nights with average cadence of 1.349 days.

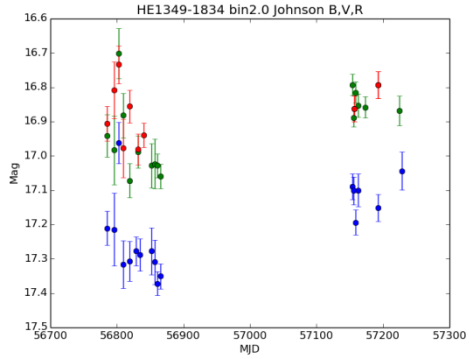

Figure 5 Variability of HE1349-1834 in Johnson B, V, and R filters

As presented in Figure 5, the light curves of HE1349-1834 shows good variability. According to Johnson B curve, there are two significant increases by MJD 56800 to MJD 56850, and another dramatic one around MJD 57150.

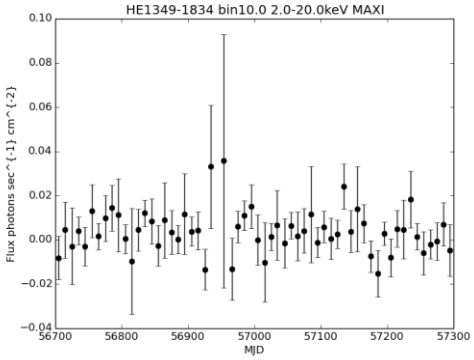

Figure 6 Variability of HE1349-1834 at X-ray in 2.0-20.0 keV band

As shown in Figure 6, the X-ray light curve of HE1349-1834 cannot be observed clearly as the data comes up with large error bars. However, it seems to illustrate an M-shaped variability pattern around MJD 56750-56850 and another peak around MJD 57150 which may relate to the optical data at that time.

Short-term Variability of HE1417-0909

HE1417-0909 has B_j = 17.19 with redshift 0.044. The data covers around 134 observing nights with a cadence of 1.872 days.

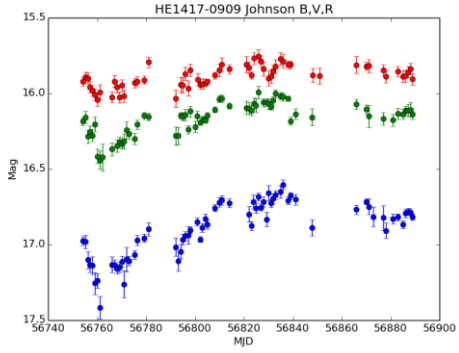

Figure 7 Variability of HE1417-0909 in Johnson B, V, and R filters

In Figure 7, variability of HE1417-0909 in Johnson B, V, R is certainly seen: the curve sharply fall of 0.5 magnitude to MJD 56760 then raises gradually to MJD 56820, significantly seen in Johnson B. There is another drop about 0.25 magnitude around MJD 56830 and MJD 56880 as seen in Johnson R and B respectively.

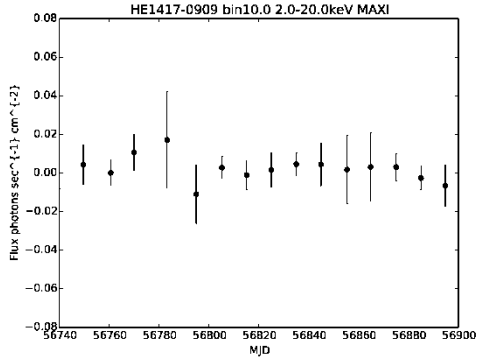

Figure 8 Variability of HE1417-0909 at X-ray in 2.0-20.0 keV band

As performed in Figure 8, the X-ray light curve of HE1417-0909 is not as thick as in Johnson B, V, R and does not show significant variability. Despite the data contains large error bar, there are a moderate increase about MJD 56780 and a small increasing pattern by MJD 56800 to the end of observation which may relate to the optical data.

Short-term Variability of HE1519-0634

HE1519-0634 has B_j = 17.06 with redshift 0.082. The data covers around 144 observing nights with average cadence of 2.13 days.

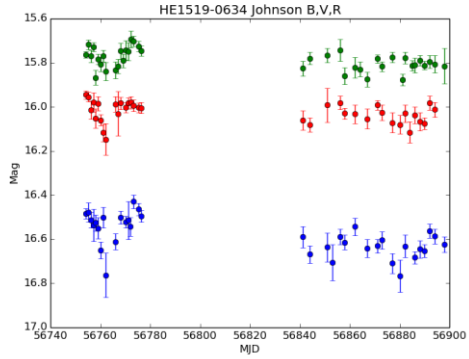

Figure 9 Variability of HE1519-0634 in Johnson B, V, and R filters

In Figure 9, variability of HE1519-0634 in Johnson B, V, R is obviously observed as showing a dramatic drop around MJD 56760 with approximately 30-day period and another moderate one around MJD 56880 with.

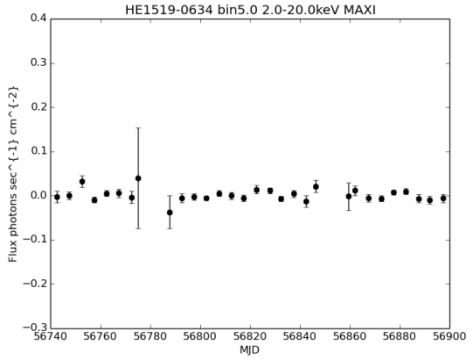

Figure 10 Variability of HE1519-0634 at X-ray in 2.0-20.0 keV band

In Figure 10, the light curve of HE1519-0634 at X-ray is not as dense as in Johnson B, V, R. The graph seems fluctuated and has no decrease around MJD 56760 and 56890 like the optical one.

Conclusions

We used 0.6m Thailand's robotic telescope to monitor 30 AGNs and found 6 objects with obvious variability at visible wavelength which is 20% of our samples.

From characteristics of light curves at both wavelengths exposed in this study, one in visible light using photometric monitoring shows exacts variability of the target AGN; it further shows significant peak or drop which is possibly a sign of outburst occurring at that time. The X-ray light curve, in contrast, shows little variability since the resolution of MAXI and its sensitivity is not so good. As flux from HES objects is too faint for MAXI, we cannot verify either signs of outburst or the relation between variability at visible light and X-ray from this study.

Despite the optical data shows good variability, the observation can be incomplete in case of daylight or moonlight, climate, or telescope maintenance, resulting in lack of variability observed in the missing period. To complete the light curve, information from other telescopes may be added. Since MAXI is an on-board device, it can obtain X-ray data from the target without any obstacles as found on terrestrial telescope thus the X-ray light curve is mostly continuous throughout observing time.

In next study, we should monitor objects which already show X-ray burst e.g. NGC2110 but has not yet been followed up in the visible wavelength.

Acknowledgments

We would like to thank to National Astronomy Research Institute, Thailand (NARIT) and University of North Carolina about offering us to use Thailand's robotic telescope time. We would like to thank to JAXA who give the MAXI data for public. Finally, we would like to thank to Ubon Ratchathani University and SPC2016 for the opportunity to publish this study.

References

[1] Schulze A, Wisotzki L, Husemann B. Low redshift AGN in the Hamburg/ESO survey. I. The local AGN luminosity function. A&A 2009; 507 (2): 781-793.

[2] Ueno S et al. MAXI Light Curves of Non-Blazar Type Active Galactic Nuclei. Proceedings of the First Year of MAXI: Monitoring Variable X-ray Sources, Poster Presentations, 4th International MAXI Workshop; 2010 Nov 30 - Dec 2; Tokyo, Japan [cited 2015 Sep 20]. Available from: http://maxi.riken.jp/FirstYear/abstbook_web_20101108.pdf.

[3] Vijarnwannaluk B, Schramm M, and Rujopakarn, W. Photometric Monitoring of Active Galactic Nuclei using Thai Robotic Telescope in Chile [Internet]. 2015 [cited 2015 Sep 20]. Available from: https://twiki.cern.ch/twiki/bin/view/Main/SPC2015Proceedings.

[4] Wisotzki L et al. The Hamburg/ESO survey for bright QSOs. III. A large flux-limited sample of QSOs. A&A 2000; 358: 77-87.

Photometric Reverberation Mapping of Quasar HE0345+0056

B. Vijarnwannaluk[1*], M. Schramm[2] and W. Rujopakarn[1,3]

[1]Department of Physics, Faculty of Science, Chulalongkorn University 254 Phyathai Road, Patumwan, Bangkok Thailand 10330

[2] National Astronomical Observatory of Japan (NAOJ), 2-21-1 Osawa, Mitaka, Tokyo 181-8588, Japan

[3]Kavli Institute for the Physics and Mathematics of the Universe (Kavli IPMU),5-1-5 Kashiwanoha,Kashiwa, 277-8583, Japan

E-mail: Bovornpratch.v@student.chula.ac.th

Abstract

We have analyzed photometric and spectroscopic data of HE0345+0056 which is an AGN in our ongoing variability monitoring program. Our well defined parent quasar sample is drawn from the Hamburg/ESO survey and observed in several broad- (B, V, R) and narrow-band filters with the Thai Robotic telescope in Chile. Our aim is to use photometric reverberation mapping techniques to study the BLR of our AGNs. Data reduction was done using a python based pipeline we created using publicly available software to extract the photometry in order to create light curves used in our analysis. During our observation in 2014 we have found a change in HE0345+0056 magnitude of approximately 0.1 mag in broadband BVR over 300 days extending from late August to today (MJD 56880-today) with high cadence. A follow-up spectroscopy observation started at the same time at the Higashi-Hiroshima Observatory. Spectroscopic data of 8 epochs were obtained for analysis in order to confirm the photometric results. Here we present the results of the photometric and spectroscopic analysis and also the results from our photometric reverberation mapping using NB filters. We obtain a time lag of 30 ± 5 days, corresponding to the Hβ broad line region size as 30 ± 5 light days. Using a single epoch spectra, we also obtain the SMBH mass of 39 ± 6 million solar mass.

Keywords: Glass, Photometric reverberation mapping, Photometric monitoring, BLR, SMBH

Introduction

Active galaxies are galaxies with extremely bright luminosity throughout the electromagnetic spectrum. The source of this luminosity is the Active Galactic Nuclei (AGN) which houses a Super Massive Black Hole (SMBH) at its core. Around the SMBH is a dense disk of material constantly falling in to the SMBH, the process also known as the Accretion Process powers the extreme luminosity which usually outshines the SMBH host galaxy either totally or partially. AGNs have been a center of the study of galaxy evolution and a key parameter in understanding how the process works is the mass of the SMBH at the center. Reverberation mapping [1] techniques have been successful in determining the mass of AGNs whenever an AGN outburst occurs. However, the technique requires constant spectroscopic observation which requires a lot of telescope time. Hence, a carefully selected list of targets is usually required.

An alternative approach to reverberation mapping is photometric reverberation [2] mapping. In addition to broad band observations, narrow band data is used to observe the response of the BLR when an outburst has occurred. The use of narrow band filters instead of spectrum allows small robotic telescopes to observe a larger number of targets in less time under a smaller budget.

The narrow band data is calibrated and cross correlation is employed between the broad band light curve and narrow band light curve to find the time tag between the two signals. When the time lag is obtain, we are then able to make estimations of the BLR size through the same process as reverberation mapping. When data from spectroscopy is included, the SMBH mass may be estimated using Keplerian mechanics. In our study, we

have used a group of robotic telescopes station at the Cerro-Tololo Inter-American Observatory (CTIO) to observe a group of low-redshift quasars. Here, our main objective is to investigate wherever photometric reverberation mapping techniques may be applied to the photometric data obtained from our observation and to estimate the Broad-line region size and the black hole mass of the target AGN.

Materials and Methods

The Target

HE0345+0056 is a quasar from a well-defined sample at z < 0.3 selected from the Hamburg/ESO survey [3]. Table 1 shows some properties of the quasars. The Hamburg/ESO catalog is a wide-angle survey of quasars in the southern sky using the ESO 1-meter telescope and its 4-degrees prism at the La Silla observatory in Chile.

Table 1 Characteristics of HE0345+0056

α(J2000)	δ(J2000)	$B_j$mag	L_{bol}	z
$3^h47^m40.2^s$	$+01^o05'14.3$	14.86	$10^{44.7}$	0.029

For our on-going photometric monitoring campaign we have selected about 150 out of 330 quasars at z < 0.3 plus an extended list with redshifts up to z = 1.

The Photometric Data

Photometric data was obtained using the Thai Southern Hemisphere Telescope (TST) also known as PROMPT8 from August 12, 2014 to today. PROMPT8 is a 0.6 ritchey chretien telescope with a field of view of 30 arcmin; controlled through a PHP website called Skynet. In our study, we used broadband Johnson B, V and R to monitor outburst. Since the H-Beta emission line is shifted into the coverage of the narrow band [OIII] at 5007 Angstrom, we used narrow band [OIII] to monitor the responds of the BLR.

The Spectroscopic Data

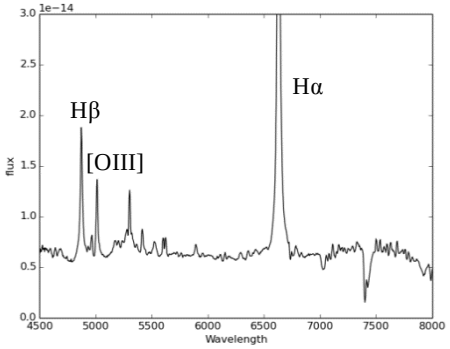

Figure 1 Spectrum of HE0345+0056

Spectroscopic data was obtained in order to confirm the change in the H-beta emission line (see Figure 1). Observation was done at the Higashi-Hiroshima Observatory in Japan during August 20th 2014 to October 3rd 2014 using the telescope's HOWPoL polarimeter which also functions as a low-resolution spectrograph with R = 400.

Data Reduction

In our study, we preform both absolute calibration and relative calibration to the data. Data reduction is done using an improved python pipeline [4] and publicly available software. For the spectroscopic data we used IRAF packages to obtain the long slit spectrum. Our Aim is to calibrate both broad band photometric data and narrow band [OIII] data in order to preform cross correlation between both to obtain the time lag of the Broad line region.

Photometric Data Analysis

Basic image calibration including Dark and Bias subtraction and flat division is done automatically by Skynet's system. The python based pipeline uses SWARP [5] to stack the images and SExtractor [6] to extract the objects in the field. A filtering process is them used to filter out bad observations including observations in which our target reside outside our field of view and those in which the targets signal to noise ratio is less than 12. We will

only use those observations that pass the filter in our analysis.

Relative photometry is done by calibrating the flux of the object in respect to another. Here, we calibrate our quasar in respect to calibration stars from the SDSS-III DR9 catalog. We took care to eliminate potential variable stars from our calibration. A median scaling factor of the calibration stars is also calculated and used to adjust the fluxed. Using the zero point calculated from absolute photometry we calculate the magnitudes and obtain the relative light curve.

Absolute photometry is done by calibrating the magnitude to those of a known catalog. Here we use bright stars from SDSS-III DR9 catalog that have a magnitude between 12 and 16 and are present during the whole observation epoch as our reference stars. Also, we only use the point-spread function magnitudes (PSF mags) from the catalog; magnitude conversions from SDSS u,g,r,i,z to Johnson BVR were done using equations from Lupton 2005 for stars and Jester 2005[7] for quasars more information can be found at http://www.sdss.org/dr12/algorithms/sdssUBVRITransform/.

After calculating the zero point of all reference stars a sigma clipping is applied to cut off extreme outliner stars. The median zero point of the remaining reference stars' is then used to represent the observation night and the error is based on the 25/75 percentiles. We ensure that at least ten stars go in to the final zero point estimation. Magnitudes and errors are then calculated.

Narrow band Photometry

The purpose of the narrow band data is to capture the change of the Hβ emission line by using a photometric filter instead of doing spectroscopy. Therefore, we must check if we can separate the [OIII] flux of the AGN from the continuum fluxes. In this case, we first create a calibrated color diagram of NB vs. V-NB.

As shown in Figure 3, we see a clear excess in the NB filter in respect to the broad V-filter indicating that the Hβ line is dominating the [OIII] filter. We preform both absolute calibration and relative calibration to our NB data. Since we cannot define a narrow band zero point we create and absolute photometry light curve in respect to the V band light curve by calculating the V – NB magnitudes in each observation night then plot a light curve.

Relative photometry for the narrow light curve is done using the same idea as the broad band relative light curve. Using reference stars that are present in the field during the whole observation we compute the scale factors and the median scale factor and apply it to the quasar fluxes. Without using a zero point we calculate the magnitudes and obtain the light curve.

Spectroscopic Data Analysis.

Our spectroscopic data was reduced using standard long-slit procedures with IRAF. Dispersion line extraction was done using *apall* to convert 2D spectrum to 1D spectrum. Wavelength calibration was done using sky glow lines and flux calibration was done using standard star HR1544.

Results and Discussion

Photometry

Using Broadband BVR filters to observe our target and a python based pipeline we are able to obtain a set of BVR light curves using both absolute and relative photometry with high cadence over a span 300 days with an approximate 2 day cadence (see Table 2).

Table 2 Observation statistics of HE0345+0056

Filter	Total Epochs	Good Epochs	<Cadence>
B	157	155	1.94
R	151	150	2.02
V	165	161	1.88
OIII	147	146	1.97

.

Using our data we preform both absolute calibration and relative calibration. Figure 2 shows the absolute

photometry light curve in all bands. Through absolute calibration, we obtain obtained a median magnitude of 14.62, 14.61, and 14.03 in B R and V respectively in the range listed in Table 3.

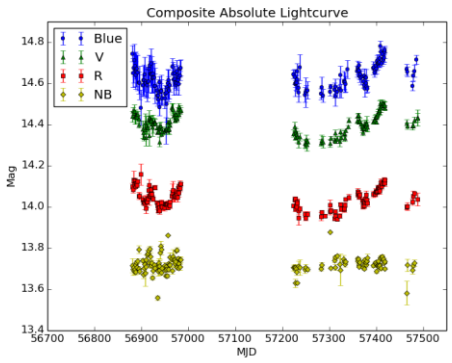

Figure 2 Absolute calibration light curve in BVR and [OIII] from top to bottom. Magnitudes are offset by -0.2 in V and +13.3 in [OIII]

Table 3 Absolute calibration Magnitude range

Filter	Mag[1]
B	14.55 - 14.70
R	14.53 - 14.67
V	13.98 -14.11
OIII - Continuum	0.38 - 0.45

[1] 10th percentile mag – 90th percentile mag

The typical errors that we achieve in our absolute calibration for each night is approximately 0.04 mags in B band while in V and R band we achieved errors of 0.02 mags.

Relative photometry is employed to improve the calibration by calibrating the quasar against stars from the SDSS catalog. Typically, we use six to ten stars per filter in our calibration. Figure 3 shows the results of our relative calibration. The magnitudes we obtained using Relative photometry with a median scaling factor is 14.61, 13.89 and 14.54 in B R and V respectively. Figure 4 shows that our quasar has a clear H-beta emission from the AGN inside which is not from the stars in the host galaxy.

Here we see a change in the magnitudes with amplitudes about 0.6 in all filters. The range of change using relative calibration is larger than absolute calibration and maybe a sign of problems in our calibration.

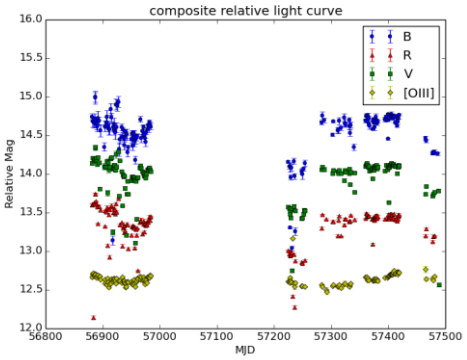

Figure 3 Relative calibration light curve in BVR and [OIII]. Magnitudes are offset by -0.5 in R, -0.5 in V and +22.5 in [OIII]

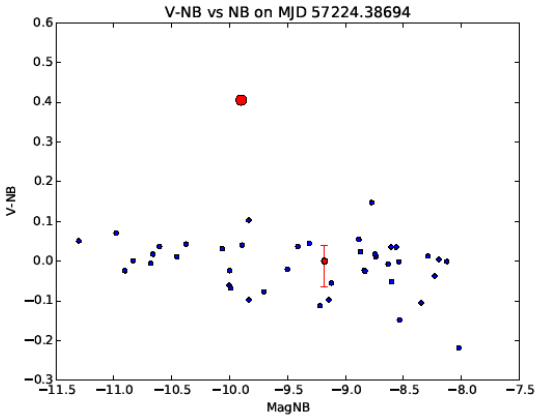

Figure 4 Example of the target color offset. The excess in the NB filter originated from the strong Hβ emission. The offset is 6.5σ from the stars median.

Broad and narrow band cross correlation

In order to extract the time lag of the narrow band light curve in comparison of the broad band light curve, cross correlation is employed between both filter bands. Following similar studies such as Nunez et al. 2013 of using cross correlation. We found that in cross correlation between broad band light curves we obtained no time lag for the correlation. However, by cross correlating the absolute B Broad band light curve and the narrow band light curve we found a time lag of 26 ± 10 days as shown

in Figure 5. Errors are defined by the FWHM of the correlation peak.

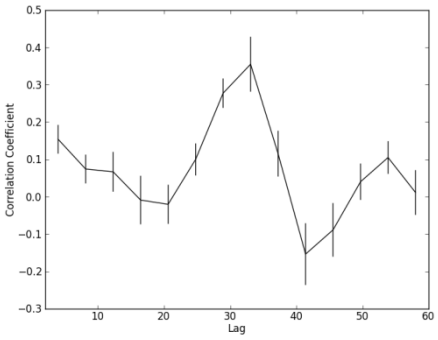

Figure 5 Cross correlation between B/NB

After subtracting the continuum from the NB data we obtained a time lag of 30 ± 5 days. The time lag we obtain is in agreement with the R_{BLR}-L relationship in Bentz et al. 2009 [9] shown in Figure 6. When considering the luminosity of our target AGN.

However, the 8 epoch spectroscopic data we currently have is not sufficient enough to confirm the photometric time lag. Therefore, we are currently trying to extend the spectroscopic campaign to confirm the time lag and SMBH mass.

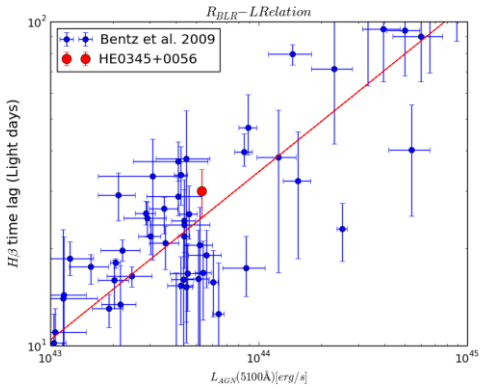

Figure 6 R_{BLR} – L plot using data from Bentz et al. 2009 with best fit of the power law α = 0.519 Our data is the red dot.

SMBH Mass Estimation

The virial theorem provides us with an equation to find the mass of the SMBH which is given by

$$M = f\frac{R_{BLR}\sigma_{BLR}^2}{G} \quad (1)$$

Where *f* is a constant which depends on the BLR shape and Kinematics usually taken as unity but studies suggest otherwise. Here we adopt *f* as 5.5 ±1.7 as defined in Onken et al. 2004 [10]. We obtain velocity dispersion directly from the Hβ line shown in Figure 7 as 789.49457 km/s. This dispersion and the BLR size of 30 ± 5 light days give us the SMBH mass of Log M_{SMBH} = 7.06 ± 0.436. The mass we obtain is in agreement with previous calculations [11]

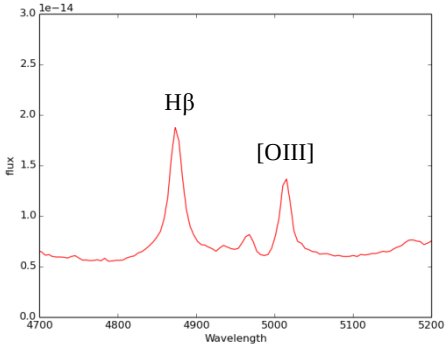

Figure 7 Enlarged spectrums at Hβ region

Conclusions

We conclude that photometric reverberation mapping is promising technique to study AGNs through the Thai Southern Hemisphere Telescope (TST) and we shall implement this technique to our AGN variability program. From our study of HE0345+0056, We have produced results using the telescope to study HE0345+0056 and obtained the BLR size as 30 ± 5 light days and the SMBH mass as Log M_{SMBH} = 7.06 ±0.436. The mass we obtained is in agreement with previous calculations. Our next step is to improve our analysis to obtain more accurate results.

We are looking into ways to improve our results. First we will continue to obtain more data to improve the photometric time lag. As stated before, the 8 epoch spectra we obtained could not confirm the photometric time lag, therefore we are trying to continue the spectroscopic campaign to confirm the time lag through spectroscopy. Since this is just a test case, we plan to

extend this procedure to the full sample of 150 quasars and see if we may obtain a R_{BLR} – L relation using our sample.

Acknowledgments

We would like to thank the PROMPT telescope team at the University of North Carolina, the National Astronomical Research institute of Thailand for the use of the PROMPT telescopes in Chile and the Higashi-Hiroshima Observatory for the spectroscopic analysis.

This project made use of the Vizier database at Strasburg, France, data analysis tools such as SWARP and SExtractor and the SDSS3 DR9 catalogs.

References

[1] Blandford, R. D. and McKee, C. F. 1982. "Reverberation mapping of the emission line regions of Seyfert galaxies and quasars". **The Astrophysical Journal**. 255:419

[2] Haas, M., et al. 2011. "Photometric AGN reverberation mapping – an efficient tool for BLR sizes, black hole masses, and host-subtracted AGN luminosities". **Astronomy & Astrophysics**. 535: A73

[3] Wisotzki, L.,et al. 1996. "The Hamburg/ESO survey for bright QSOs. I. Survey design and candidate selection procedure". **Astronomy & Astrophysics Supplement**.115:227

[4] Vijarnwannaluk, B., Schramm, M. and Rujopakarn, W. 2015. "Photometric Monitoring of Active Galactic Nuclei using the Thai Robotic Telescope in Chile". **SPC 2015**. *AST 18-21*

[5] Bertin et al. 2002. "The TERAPIX Pipeline". ASP Conference Series. 281:228

[6] Bertin, E. and Arnouts, S. 1996. "SExtractor: Software for source extraction". **Astronomy & Astrophysics Supplement**. 317:393

[7] Jester, S., et al. 2005. "The SDSS View of the Palomar-Green Bright Quasar Survey". **The Astrophysical Journal.** 130:873

[8] Nunez, F., et al. 2013. "Photometric AGN reverberation mapping of 3C120". **Astronomy & Astrophysics.** 545:A84

[9] Bentz, Misty C., et al. 2009. "The Radius-Luminosity Relationship for Active Galactic Nuclei: The Effect of Host-Galaxy Starlight on Luminosity Measurements. II. The Full Sample of Reverberation-Mapped AGNs". **The Astrophysical Journal**. 697:160-181

[10] Onken, C. A., et al. 2004. "Supermassive Black Holes in Active Galactic Nuclei. II. Calibration of the M-sigma Relationship for AGNs". **The Astrophysical Journal. 615: 645-651**

[11] Schulze, A.,et al. 2010. "Low redshift AGN in the Hamburg/ESO Survey: II. The active black hole mass function and the distribution function of Eddington ratios ?". **Astronomy & Astrophysics**. 516:A87

Study of Orbital Elements of Asteroids in Cometary Orbits Using 2.4 m and 0.7 m Diameter Telescopes

S. Deantakhu[1,2*] and S. Wannawichian[1]

[1] Department of physics and Materials Science, Faculty of Science,
Chiang Mai University, Chiang Mai, Thailand

[2] National Astronomical Research Institute of Thailand (NARIT),

*E-mail: sittiporn666@gmail.com

Abstract

The orbital elements of asteroids in cometary orbits are studied by using 2.4 m and 0.7 m diameter telescopes base on celestial coordinate from asteroid images. The study uses Astrometry technique to find real position of asteroid in space and calculate its orbitals element. This work focuses on asteroids with high variation in position. We select asteroids that have Tisserand's parameters [1] T_j < 3 and are disturbed by the gravity from Jupiter. Orbital element and the Minimum Orbital Intersection Distance (MOID) [2] are calculate and compared with astrometry result of other observations from Minor Planet Center database.

Keywords: Asteroid, Orbital element, Comet

Introduction

Asteroid is given much attention because it has a chance to impact Earth. The accurate calculation of asteroid's position necessary for the protection plans from extinction and for studying nature of this celestial body. Asteroid position can be perturbed by many factors. The gravity from giant planet such as Jupiter is one of them. The aim of this work is to study orbital element of asteroids which move in cometary-like orbit with astrometric data from 0.7 and 2.4 m telescope. The result must be calibrated by comparing with data from other observations which are included in database of Minor Planet Center. Orbital elements (MPC) are importance parameters are used to generate ephemeris for asteroid monitoring. Determination of asteroid orbital element was introduced by Gauss (1801) [3], following with least square fitting. This method was proved by Mazzi (1801) [3]. During the discovery first dwarf planet, Ceres. Currently Gauss's method is still used for determination of orbital elements of many hundred thousand asteroids with data from many observations taken place all over the world. As a result, applying statistical method on the data allows the calculation of asteroid position to be much more precise.

Materials and Methods

Observation and Data Analysis

Astrometric data in this study was obtained from visible images, which were taken by 0.7 and 2.4 m telescopes at Thai National Observatory (TNO). Continuous observation provides information of asteroid's positional change. The actual coordinates of asteroids from raw image were analyzed by using World Coordinate System (WCS) [4] software. In order to acquire precise positions of asteroids, matching and calibration procedure are accessory. Change of asteroid's position in each image was determined by image processing technique. Variation of asteroid position is used to calculate its orbital elements via Gauss method [5]. Finally asteroid's coordinate and orbital elements from this work will be compared with database in Minor Planet Center (MPC), in order to find standard derivation of our observation from the database.

For each orbital element parameters be calculate by equation

Where

$$e \sin \upsilon_1 = \frac{(l/r_1 - 1).\cos 2f_2 - (l/r_2 - 1)}{\sin 2f_2} \qquad (1)$$

e is eccentricity, v_1 is True anomaly for position 1 r_1 and r_2 radius vector polar coordinate for position 1 and 3, l is semi-letus rectum,and f_2 from .

$$a = \frac{l}{(l-e^2)} \quad (2)$$

where a is Semi-major axis .

$$\sin\omega \sin i = P_z \cos\varepsilon - P_y \sin\varepsilon \quad (3)$$

and

$$\cos\omega \sin i = Q_z \cos\epsilon - Q_y \sin\varepsilon \quad (4)$$

where ω is Argument of perihelion, i is Inclination, ε is Angle between Ecliptic plane and Celestial plane $P_x, P_y, P_z, Q_x, Q_y, Q_z$ and R_x, R_y, R_z are values of heliocentric equatorial coordinate vector in heliocentric plane-of-orbit.

$$\sin\Omega = (P_z \cos\varepsilon - P_y \sin\varepsilon)\sec\varepsilon \quad (5)$$

and

$$\cos\Omega = P_x \cos\varepsilon - Q_x \sin\omega \quad (6)$$

where Ω is Longitude of Ascending node.

$$\cos i = -(P_x \sin\omega + Q_x \cos\omega)\csc\Omega \quad (7)$$

and

$$D^2_{min} = \frac{X_0^2 a^2 (1-e^2)\sin^2 i}{2a-1-a^2(1-e^2)\cos^2 i} \quad (8)$$

where D^2_{min} is MOID, X_0 is distance from starting to end point in reference plane.

Results and Discussion

The observed asteroid position of the observation is show in Figure 1. With Software for Calibrating Astrometry and Photometry (SCAMP) shown in Figure 2, we receives the coordinates of asteroid 2000 UR27 and its orbital elements, After the use of astrometric model of obtain the asteroid's orbital elements, the result was compared with the database in MPC, show in Figure 3.

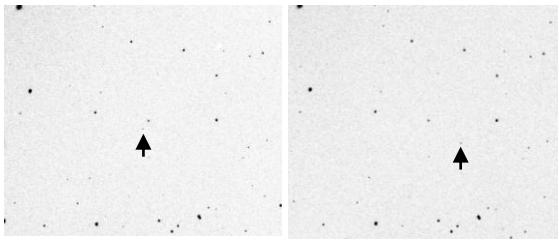

Figure 1 Asteroid 2000 UR27 moved across the sky with difference apparent angular velocity from stars in the background. Differential technique provides asteroid's movement.

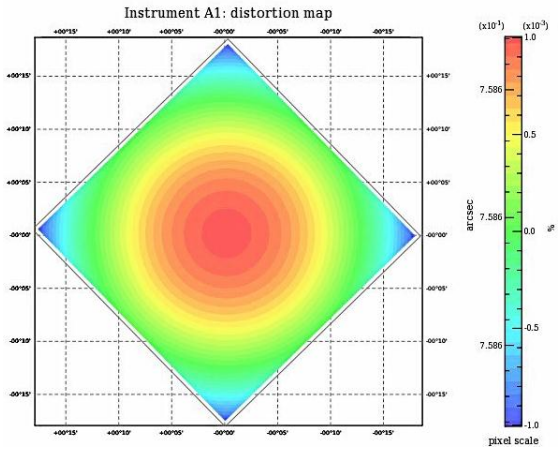

Figure 2 Map of pixel scale from 0.7 m telescope show astrometric instrument and astrometric model of the input frame after calibration.

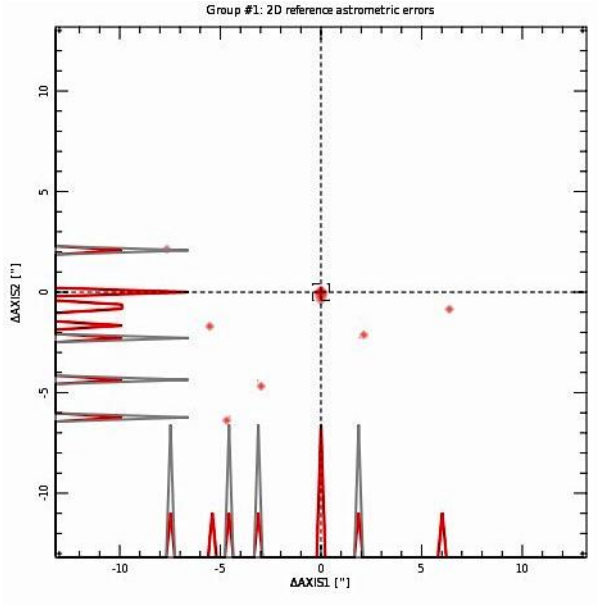

Figure 3 The differences between coordinates of overlapping detections. When using The Two Micron All Sky Survey (2MASS) catalog. The differences display the variation of asteroid coordinates.

This study uses fifteen asteroids which have T_j < 3 with Low $MOID_E$ (0.05<). Near Earth Asteroids (NEA) are generated for ephemeris by MPC database from observations as show in Table 1. From example of our observations, the orbital elements of 2000UR27 asteroid were shown in Table 2. From the raw image shown in Figure 1, the distortion map in each pixel was analyzed. In Figure 2, the round shape represents the 3rd degree polynomial distortion, which is sufficient for most observations. However the Position Angle (PA) was

calibrated by using appropriate catalog for better in future observation.

Table 1 List of Asteroids in the observations with some asteroids under the determining of $MOID_{Earth}$

Asteroid	T_j	$MOID_{Earth}$
(306367) Nut	3.0	0.05273
1973 NA	2.5	0.08983
1998 SO10	2.9	0.45573
(7092) Cadmus	3.0	0.09743
1994 AH2	3.0	0.10163
1998 MT24	3.0	0.14224
1999 JM8	3.0	0.0437
1999 TF211	3.0	0.01963
2000 NM	2.9	0.13018
2000 UR27	3.3	
2002 JB9	2.5	0.03207
2003 KP2	2.6	0.15848
2004 JN13	2.8	0.1318
2007 HA59	2.6	0.28621
2010 JG123	3.0	

Table 2 Result from observation and calculation of 2000UR27

2016/5/12		
JD	RA	DEC
2457521.1209143517	10 13 04.99	08 01 48.2
2457521.1280555557	10 13 02.12	08 02 47.3
2457521.1352083334	10 13 02.56	08 04 51.6
n = 0.96833519	Peri. = 93.79497	
a = 1.01185645	Node = 232.41782	
e = 0.0415270	Incl. = 2.03650	
P = 1.02/371.77d	q = 0.969837	
Q = 1.05387589	MOID = 0.0013	

Conclusions

Several observations are necessary for determination of asteroid orbital elements by Gauss method. However, some observations some error in the calculation of orbital elements from mean value. The Väisälä orbit method [4] was used to improve uncertainty in our calculation. Because the error in our calculation remains significant, our future work will focus on improving the calculation of the asteroid's orbital elements.

Acknowledgments

We would like to thank you National Astronomical Research Institute of Thailand (NARIT), Minor Planet Center (MPC). "www.projectpluto.com" Dr. Saran Posyajinda, Dr. Ayung-Jin Kim and Dr. Utane Sawangwit.

References

[1] Tancredi, G., 2014. A criterion to classify asteroid and comet based on orbital parameter, Icarus, 234, 66-80.

[2] Bonanno, C., 2000. An analytical approximate for the MOID and it consequences, Astronomy and astrophysics, 306,411-416.

[3] Bowell, E., Virtanen, J., Muinonen, K., And Boattini, 2002. "Asteroid Obit Computation", Asteroid III The Arizona Board of Regents, 27–43.

[4] NASA., McGlynn, T., 03 May 2016, Website: http://fits.gsfc.nasa.gov,

[5] Grinch, G. 2004 "Classical and modern orbit determination for asteroids". Proceedings IAU Colloquium, No. 196

[6] Fitzpatrick, R., Website: http://fits.gsfc.nasa.gov, 2 November 2015

Locating of Meteorite from Fireball in Thailand on 7th September 2015 by Contrail Calibration with Coordinates of Background Stars

T. loylip[1*] and S. Wannawichian[1,2]

[1]Department of physics and Materials Science, Faculty of Science, Chiang Mai University, Chiang Mai, Thailand

[2]National Astronomical Research Institute of Thailand (NARIT), Chiang Mai, Thailand

*E-mail: teerayut@Narit.or.th

Abstract

Fireball is the extremely bright meteor, which could be asteroid, comet or near Earth objects (NEOs) falling through Earth's atmosphere, heated and glowed from the collisions with particles in the atmosphere. Its contrail appears like a long tail of smoke in the sky. The remains of burning object in atmosphere impact onto the ground. The residue of burring meteor is called "Meteorite". Astronomers can search fragments of the meteorite by compare contrail's images with background stars images that were taken from the same place to determine the location of the meteorite impact and collect observing data from eyewitnesses of fireball. From this information we may confirm the direction of fireball and burning tail of the meteorites. From fireball which appeared in Thailand since September 7, 2015, we can estimate the contact point by comparing photo of contrails to background star. The contact point could located in Sai Yok national park, Kanchanaburi province, Thailand. That would lead us to be able to find parts of meteorite in that area. This research reports the proceeding of meteorite explore which might remain in that area.

Keywords: Fireball, Asteroid, Comet, Near Earth Objects (NEOs), Meteorite, Contrail

Introduction

The Meteors or meteor showers are glowing fragments of objects from outside Earth's atmosphere that burn and glow while entering Earth's atmosphere. The objects could be asteroids, comets or near Earth objects. Very bright meteor is called a fireball. A fireball is another term for a very bright meteor, generally brighter than magnitude -4, which is similar to the brightness magnitude of Venus in the morning or evening sky. Sometimes you can see fireballs in daytime. For this interesting event, because the object is large, some of fragment survive the burning and impact into earth's surface, becoming a meteorites. The falling of meteorites to the Earth's surface is part of Earth accretion process from dust and rocks in solar system. When these fragments come close enough to Earth to be attracted by its gravity. They may fall into Earth. As we see the evolution of life on Earth has been affected by the impact from these space objects. When a large object impacts the surface of Earth, the rocks at the impact site are deformed and some of it is ejected into the atmosphere and fall back to the surface. This results in a bowl shape depression with raised rim, which called an impact Crater. Astronomers discovered the Impact crater to be an evidence of impact a tool help to find meteorite fragments.

But nowadays, with advance of technology, the camera becomes important recording device for these phenomena. We can use such information for the calculations of falling meteorite. With fireball events in Thailand on September 7, 2015, we are searching for the falling site of the meteorite by using the same methods to find meteorites in Russia and Sudan.[1,2] From Fireball event, astronomers discovered the impact crater to be an evidence of impact and help to find meteorite fragments. With fireball events in Thailand on September 7, 2015, the falling site of the meteorite was searched by observing data from eyewitnesses of fireball. The calibration is done by taking star background images on site, as shown in Table 1.

Table 1 Locations, in Kanchanaburi province, of key events from the analyses of recorded videos and images.

Location	File Type	Event Observed	Latitude	Longitude
Sai Yok ,	image	Contrails	14.30306	98.99417
Lat Ya	image	Contrails	14.1011	99.4175
Srisawat	image	Contrails	14.43138	99.12972
Srisawat	image	Contrails	14.47136	99.13536
Srisawat	image	Contrails	14.47833	99.12667
Tha Muang,	video	Fireball	13.89278	99.66056

Materials and Methods

Observing data from eyewitnesses of fireball were collected. From this information we may confirm the direction of fireball and burning tail of the meteorites.

Figure 1 Star-background is calibrated from evident images captured by video recorder. The star–background was aligned by calibrating with the celestial configuration at the time of observation.

Next, images and video of fireball events that were uploaded on internet were collected. Then we calibrated direction of fireball by taking star background images on site. For calibrating video file, we need to convert video files into several images. Then image in each frame with star background images on the same site was calibrated. Stars in the background images, which are extracted into frames from video are aligned, as shown in Figure 1.

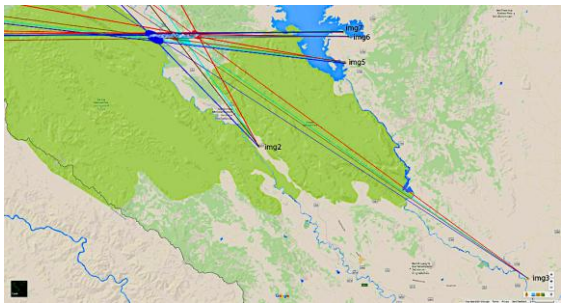

Figure 2 The trend line that indicate the trajectory of the fireball can be created**.** In the target area, we were searching for the falling trails at Sai Yok national park, Kanchanaburi Province.

For the alignment of stars in the background images, we can use this data to find the altitude of the fireball. Consequently the trend line that indicates the trajectory of the fireball can be created, as shown in Figure 2.

Figure 3 The meeting with national park's team for planning and training to prepare the process of finding a meteorite in the target area.

Next the locations of the target area are confirmed and use to find meteorite. Finally, there was a meeting with national park's team for planning and preparing the process of finding meteorite in the target area, as shown in Figure 3.

Figure 4 The team visit the area to find the meteorite, at Sai Yok national park, Kanchanaburi Province.

One along-track search was performed, with searchers spread out along a line of about 0.4 km. The signal for the team to proceed searching was started in a gravely area of the low-mass end of the strewn field, as shown in Figure 4.

Results and Discussion

For the result from meteorite recovery at the Sai Yok national park, Kanchanaburi Province, the main mass was recovered on 26 December 2015 and found to weigh 60 g, as shown in Figure 5. We found 4 fragments of the meteorite with total recovery weight about 200 g.

Figure 5 This sample is possible to be a meteorite.

Conclusions

From fireball event which appeared in Thailand on September 7, 2015, we can estimate the contact point by comparing photo of contrails to background stars. The contact point could locate in Sai Yok national park, Kanchanaburi province, Thailand. Four fragments of meteorites were found with total recovery mass about 200 g. The main mass was recovered December 26, 2015 and found to weigh 60 g. The sample is heavier than an ordinary rock and attracted to a magnet. This sample is possible to be a meteorite, and pending to further investigation.

Acknowledgments

This research project is supported by Graduate School,Chiang Mai University and the authors thank the Astronomical Research Laboratory, Department of Physics and Materials Science, Faculty of Science, Chiang Mai University.

We would like to thank National Astronomical Research Institute of Thailand (NARIT), Chiang Mai, Thailand.

We would like to thank Dr. Saran Poshyachinda deputy director, National Astronomical Research Institute of Thailand (NARIT), Chiang Mai, Thailand.

We would like to thank Mr. Matipon Tangmatitham Astronomical expertise of Michigan Technological University.

We would like to thank Group Captian Thagoon Kirdkao Learning center for Earth Science and Astronomy (LESA), Development of the Ground based Optical Satellite Observation System supported by Ministry of Science and Technology, Ministry of Information and Communication Technology and the Royal Thai Air Force.

We would like to thank Mahidol University Seismological Information Canter.

We would like to thank Astronomer Dr. Peter Jenniskens is a Research Scientist with the Carl Sagan Center at the SETI Institute and works on mission projects at NASA/Ames Research Center in Moffett Field, California, and on research topics that relate to interstellar and interplanetary matter.

We would like to thank Sai Yok national park, Kanchanaburi Province.

References

[1] Shaddad, H., Jenniskens, P., et al., The recovery of asteroid 2008TC3, Metoritics & Planetary Science, 45, 1557-1589, 2010

[2] Popova, P., Jeniskens, P., et al., Chelyabinsk Airburst, Damage Assessment, Meteorite Recovery, and Characterization, Science 342, 1069-1073 ,2013

[3] Richard, O., and Chitwood, A., Field Guide to Meteors and Meteorites,Springer,Verlag London, 2008

[4] Tatum, J.P., Tracking a fireball from eyewitness,The royal astronomical society of Canada 182, 99-177, 2005

[5] Hunnu, H., Fundamental astronomy, springer, Verlag London, 2006

[6] วิภู รุโจปการ, เอกภพเพื่อความเข้าใจในธรรมชาติและจักรวาล, นานมีบุ๊คส์พับลิเคชั่นส์, กรุงเทพมหานคร, พ.ศ 2547

[7] นิพนธ์ ทรายเพชร, มหัศจรรย์มนุษย์กับดวงดาว, จุฬาลงกรณ์มหาวิทยาลัย, กรุงเทพมหานคร, พ.ศ. 2555

[8] สมาคมดาราศาสตร์ไทย, รอบรู้ดูดาว คู่มือชมฟ้าสำหรับคนไทย, อมรินทร์พริ้นติ้งแอนด์พับลิชชิงจำกัด (มหาชน), พ.ศ. 2557

[9] ศสิพันธ์ุ คะวีรัตน์ และคณะ, การศึกษาเบื้องต้นในอุกกาบาตและเทคไทต์โดยวิธีนิวเคลียร์, การประชุมวิชาการ วิทยาศาสตร์และเทคโนโลยีนิวเคลียร์ ครั้งที่ 8, พ.ศ. 2544

[10] ระวิ สงวนทรัพย์,ปริทรรศน์แห่งเอกภพ เล่ม2, โอเดียนสโตร์, กรุงเทพมหานคร, พ.ศ. 2532

[11] ระวิ สงวนทรัพย์, ปริทรรศน์แห่งเอกภพ เล่ม 3,โอเดียนสโตร์, กรุงเทพมหานคร พ.ศ. 2532

[12] Chodas,P., and Baalke, R., Website: http://neo.jpl.nasa.gov/torino_scale, 20 September 2015

[13] Greicius, T., Dunbar, B., and Website: http://www.nasa.gov/jpl/meteorite, 10 September 2015

[14] เชิญโชค ศรขวัญ,และคณะ, เว็บไซต์:http://www.il.mahidol.ac.th/e-media, 12 พฤศจิกายน 2015

[15] Notkin, G., Website: http://www.aerolite.org/found-a-meteorite, 12 November 2015.

Developing Learning Activities on Moment of Inertia for Grade 11 Students

W. Kaewsan and U. Tipparach*

Department of Physics, Faculty of Science, Ubon Ratchathani University, Warin Chamrab, Ubon Ratchathani 34190 Thailand

* Email: udom.t@ubu.ac.th

Abstract

The sets of learning activities on moment of inertia and applications for grade 11 students were designed and created and then used for active learning activities. The activities include the experiment of the relations between linear and angular velocities, moment of inertia and related quantities, inquiry activity on rolling of objects with different shapes and radii, and law of angular momentum conservation. The results show that the students understand the concept and students' attitude towards Physics is increased.

Keywords: Learning activity, Moment of inertia, Application

Introduction

The process of teaching science focuses on students in order that the students learn and understand by constructing their knowledge. In this way, the students gain knowledge and build their scientific skills as well as social skills.

The concept of moment inertia is hard to understand for grade 11 students. It is a new and abstract concept. The text book by the institute for the promotion of teaching science and technology (IPST) does not provide enough learning activities [1]. In this work, thus, we propose developing learning activities on moment of inertia for grade 11 students to foster students so that the students can construct their own knowledge by doing learning activities such as experiments and hands-on experience.

Materials and Methods

The design of the apparatus for moment of inertia experiment is shown in Figure 1. The real set up of the apparatus is shown in Figure 2.

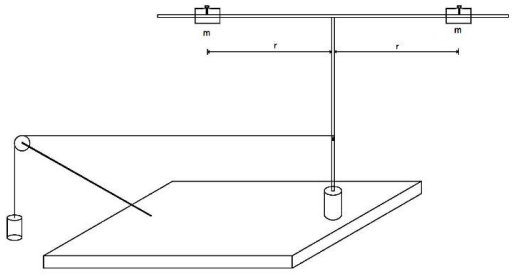

Figure 1 The diagram of the designed apparatus.

Figure 2 The real set up of the experiment for moment of inertia.

The purpose of the experiment is to construct students' concept of moment of inertia. In the first experiment, the students will carry out an experiment to verify that moment of inertia varies as the square of radius ($I \propto r^2$). In the second experiment, the students will perform an experiment to show that moment of inertia is proportional to mass ($I \propto m$).

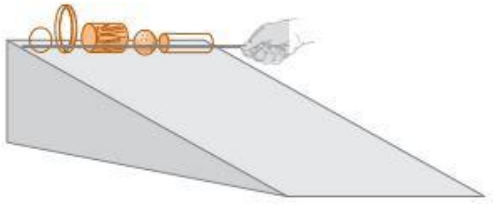

Figure 3 Bodies with different shapes roll down a ramp [3].

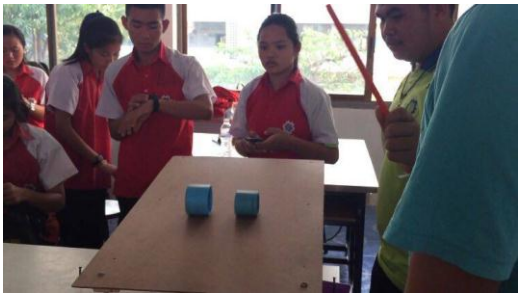

Figure 4 Rolling of objects on an inclined plane.

The third experiment will be application of moment of inertia (see Figure 4). The students perform a series of experiments using an inquiry method of teaching [2]. The inquiry question is which objects (hollow cylindrical, solid cylindrical, and solid sphere) will reach the lower end of the incline plane fastest: 1) does it depend on mass? 2) does it depend on radius? or 3) does it depend on shape? These series of experiment intend to show that the kinetic energy of rolling objects consist of rotational and translational parts. The rotational kinetic energy is $I = kmr^2$ and k depends on the shape of an object. For example, k's are 1, 1/2, and 2/5 for hollow cylindrical, solid cylindrical, and solid sphere, respectively. The fastest is a solid sphere ball because of the sphere has smallest fraction, k or smallest fraction k of moment of inertia.

The fourth experiment is demonstration the law of angular momentum as shown in Figure. 5. This demonstration show that the shorter radius of rotation, the smaller of moment of inertia, leading to the faster of the rotation.

Figure 5 The demonstration the law of angular momentum by grade 11 students

Results and Discussion

The apparatus has been used in grade 11 Physics classroom of Kudkhaopun Witthaya School. The students were excited and happy to learn. They have a chance to work in a group of 5 students. They have learned Physics by doing experiments, develop scientific skills, e.g., measurement, collecting data, graphing, analyzing data, and drawing a conclusion. They also have gained social skills such as group discussion, working together, and communication. The average score was increased with statistical significance at .05 levels as shown in Table 1.

Table 1 Mean score, average normalized gains, and t-statistics on the pre-test and post-test.

Score	Number of students	Full score (20)		SD	t
		mean	percent		
pretest	30	6.57	32.83	1.57	25.36*
posttest	30	14.70	73.50	1.76	

$t_{\alpha=.05,df\ 29} = 1.69$

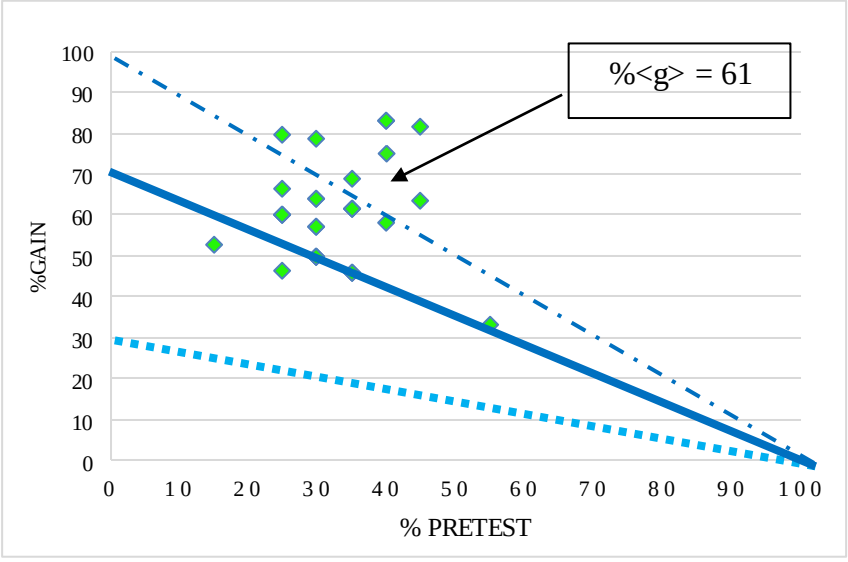

Figure 6 The relation between % Pretest and %Gain of the students.

The normalized gain, <g>, a measure of the advancement of students' learning in scores between pre-test and post-test, was expressed as a fraction of the range of possible score increase and was also calculated by[4].,

$$< g > = \frac{\%posttest - \%\ pretest}{100\% - \%pretest}$$

and

<g> < 0.3 is low gain,

0.3 < <g> < 0.7 is medium gain,

<g> ≥ 0.7 is high gain.

The average normalized gains were 0.61 which is considered as medium gain. No student is in low gain. The scores of 24 students are in medium gain and 6 students are in high gain.

Conclusions

We have developed the apparatus for learning through inquiry and active learning methods. The

learning activities helped to develop students' concepts of moment of inertia, angular momentum, and rolling. The activities also promote abilities of the student in analytical thinking on moment of inertia for the students. The students participated in Physics classroom enthusiastically. They developed scientific skills and social skills at the same time.

Acknowledgments

We would like to thank the institute for the promotion of teaching science and technology (IPST) for financial supports.

References

[1] The Institute for The Promotion of Teaching Science and Technology. 2012. **Physics Vol.2**, Ministry of Education. Bangkok. Suksapan publisher.

[2] Sanger, M.J. 2008. "How does inquiry-based instruction affect teaching majors'views about teaching and leaning science?" **J. Chem. Edu.** 85: 297-302.

[3] T. Saipin, S. Norrapoke, U. Srisakorn, G. Shuwunnasillp, and U. Tipparach "Developing Simple Experiments for Teaching Concepts of the Radius of Gyration and Moment of Inertia". **Proceedings in Siam Physics Congress 2013 May 21-23, 2013.** 405-408.

[4] R. Hake, 1998. "Interactive Enagagment VS Traditional Method: A six Thousand Student Survey of Mechanics Test Data for Introductory Physics Course", **Am. J. Phys.** 66: 64-74

Raman Spectroscopy of GaN Films on (001)- and (110)-Oriented GaAs Substrates

P. Praigaew[1], S. Sanorpim[1*] and K. Onabe[2]

[1]Department of Physics, Faculty of science, Chulalongkorn University, Phathumwan, Bangkok, 10330, Thailand

[2]Department of Advanced Materials Science, The University of Tokyo, Kashiwa, Chiba, 277-8561, Japan

*E-mail: Sakuntam.s@chula.ac.th

Abstract

Structural phases in the GaN films grown on the (001)- and (110)-oriented GaAs substrates were investigated by μ-Raman spectroscopy with the excitation wavelengths of 473, 532 and 633 nm. Raman spectra show a significant shift of phonon modes between the films on the (001)- and (110)-oriented substrates. For the (001)-oriented GaAs substrate, phonon mode of cubic-TO was clearly observed at 553 cm^{-1}. On the other hand, the films on the (110)-oriented GaAs substrates showed a higher intensity of hexagonal-E_2-high localized at 568 cm^{-1}. Furthermore, the phonon mode observed at higher wave-number is significantly shifted from 736 to 739 cm^{-1}, when the excitation wavelengths was changed from 473 and 532 nm to 633 nm, respectively. It is well known that the phonon modes localized at 736 and 739 cm^{-1} are attributed to hexagonal-A_1 (hexagonal-LO) and cubic-LO, respectively. While Raman shift of cubic-TO at 553 cm^{-1} is found to independence on the excitation laser wavelength. These results indicate that the cubic-LO phonon mode is sensitive to the excitation wavelength of 633 nm compared to other excitation wavelengths. Another possibility is due to the different of penetration depths of the laser wavelengths. It is interpreted that the GaN films exhibited more hexagonal phase in the region close to the GaN surface region. In contrast, the GaN films more dominated with cubic phase at the region near the GaN/GaAs interface.

Keywords: Raman scattering, Substrate orientation , GaN, Structural phase

Introduction

Gallium Nitride (GaN) is a promising semi-conductor materials for produce the optoelectronic devices operated in region of ultra-violet wavelengths [1]. Its alloys such as InGaN is used to produces the blue-green light emitting diode (LEDs) and laser diodes (LDs) [2-4].

GaN crystalizes in both of cubic structure (zincblend structure) and hexagonal structure (wirtzite structure), which are named c-GaN and h-GaN, respectively. It is known that c-GaN and h-GaN are wide bandgap of 3.2 eV and 3.4 eV, respectively. Since, the h-GaN crystal is thermodynamically stable, while c-GaN is meta-stable phase. Commonly, then, h-GaN is usually heteroepitaxially grown on hexagonal substrates such as sapphire [5] and Si (111) [6]. On the other hand, c-GaN with cubic phase purity of 85% has been successfully grown on cubic substrate such as GaAs (001) [7]. However, the c-GaN grown film is usually contained with h-GaN in form of stacking faults, which are constructed on (111) surface during the growth [8]. This hexagonal phase inclusion significantly effects on structural phase purity of the grown films [9].

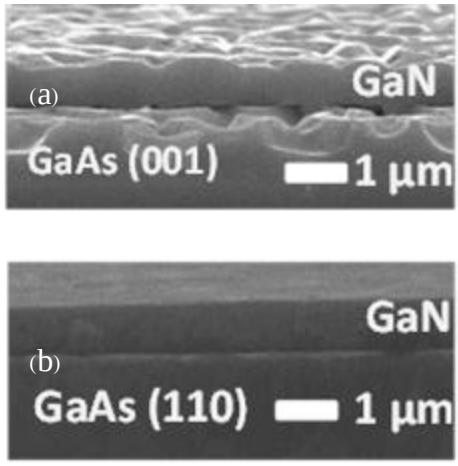

Figure 1 Cross-sectional SEM images of of (a) GaN film on GaAs (001) and (b) GaN film on GaAs (110).

To reduce a hexagonal phase inclusion, GaAs (110) surface, which has higher step density, is purposed to be a substrate for c-GaN. To analyze structural phase purity in GaN films on GaAs (110) substrates, μ-Raman spectroscopy with the excitation wavelengths of 473, 532 and 633 nm was used. Surface and interface morphologies have been investigated by scaning electron microscopy (SEM).

Materials and Methods

GaN films were grown on GaAs (001)- and (110)-oriented substrates at 900^{o}C by metalorganic vapor phase epitaxy (MOVPE). Trimethylgallium (TMGa), thertiarybutylarsine (TBAs) and dimethyl-hydrazine (DMHy) were used as the Ga, As and N precursors, respectively. Crystal structures of the GaN grown films were investigated by μ-Raman spectroscopy with the excitation wavelengths of 473, 532 and 633 nm, which expected for information from different penetration depths. Surface and interface morphologies and thickness were investigated by SEM.

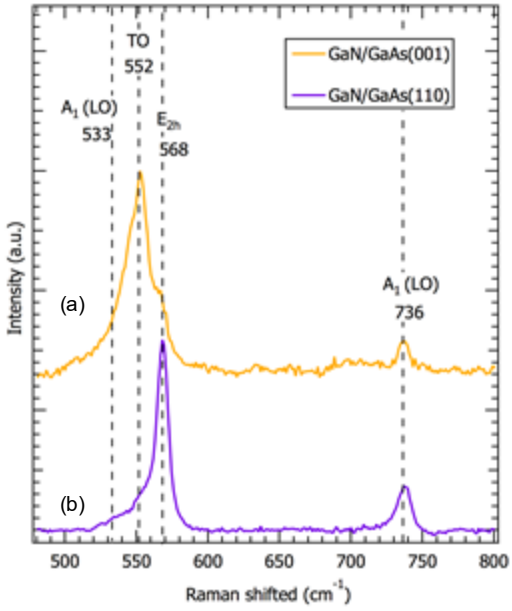

Figure 2 Raman spectra of (a) GaN film on GaAs (001) and (b) GaN film on GaAs (110) measured by excitation wavelength of 532 nm.

Results and Discussion

Figure 1 shows cross-sectional SEM images of GaN films grown on GaAs (001)- and (110)-oriented substrates. As shown in Figure 1(a), the GaN on GaAs (001) substrate exhibited a rough surface and a high density of voids at interface. These voids are due to a thermal damage of the GaAs surface at a high temperature during the growth of GaN at 900 ^{o}C. On the other hand, as shown in Figure 1(b), GaAs (110) surface with higher step density gives flat surface of GaN and a smooth GaN/GaAs interface. As expectation, this result demonstrates that GaAs (110)-oriented substrate surface, which has higher step density, can avoid the thermal decomposition of Ga-As bonds in high temperature grown. It is due to a higher nucleation of GaN on a higher step density GaAs (110) surface compared to that of GaAs (001) surface.

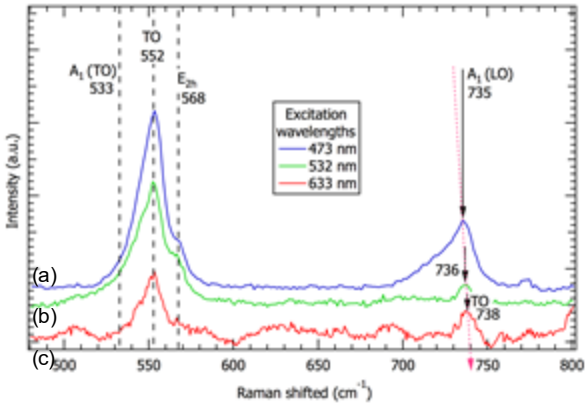

Figure 3 Raman spectra of GaN/GaAs (001) measured by excited wavelength of (a) 473 nm (b) 532 nm and (c) 633 nm

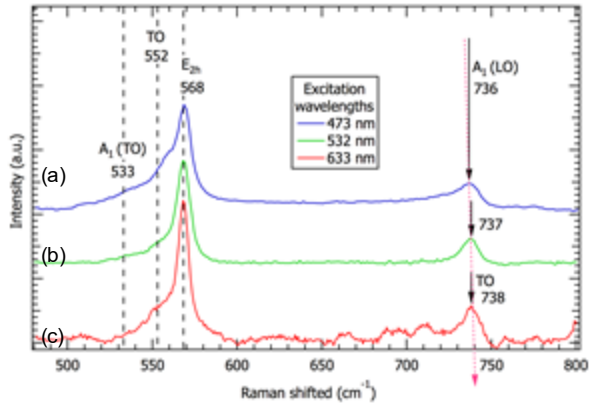

Figure 4 Raman spectra of GaN/GaAs(110) measured by excited wavelength of (a) 473 nm (b) 532 nm and (c) 633 nm

Figure 2 shows Raman spectra with excitation wavelength of 532 nm of GaN films grown on GaAs (001)- and (110)- oriented substrates. For GaN film grown on (001) substrate, Raman spectrum showed phonon mode of cubic-TO was clearly observed at 553 cm^{-1} in lower Raman shift region. On the other hand, the films on the (110)-substrates showed a higher intensity of hexagonal-E_2-high localized at 568 cm^{-1}. Hexagonal GaN phonons of A_1(TO) and A_1(LO) are observed in both spectra at 533 and 736 cm^{-1}, respectively. It is found that the hexagonal GaN phonons are sensitive to substrate surface orientation. The GaN film on GaAs (001) is dominated with cubic structure. This film was also investigated by X-ray diffraction to confirm cubic phase purity as high as 85%. On the other hand, the GaN film on GaAs (110) is dominated with hexagonal structure with a mixed cubic structure.

Figure 3 shows Raman spectra of GaN films on (a) GaAs (001)- and (b) (110)-orientated substrates with various excitation wavelengths of 473, 552 and 633 nm. For Raman spectra of GaN film on GaAs (001) substrate as shown in Figure 1(a), hexagonal GaN phonons of A_1(TO) and E_2-high and cubic-TO were clearly observed at 533, 568 and 552 cm^{-1}, respectively. The position of these phonons is found to independent on the excitation wavelength. This shown that the GaN film grown on GaAs (001) substrate is dominated with cubic structure associated with a small amount of hexagonal phase inclusion. For the GaN film on GaAs (110) substrate, as seen in Figure 3(b), the hexagonal GaN phonons of A_1(TO) and hexagonal-$E_{2\text{-high}}$ and cubic-TO phonon are observed at the same position as observed for the GaN film on GaAs (001) substrate. However, Raman peak intensity of the cubic-TO phonon is significantly decreased. This implies that the GaN film grown on GaAs (110) substrate has hexagonal structure as a main crystal structure, associated with some of cubic phase inclusion.

Additional, the Raman peak related to hexagonal GaN phonon of A_1(LO) was clearly observed at 735±1 cm^{-1} for both of GaN films grown on GaAs (001)- and (110)-oriented substrate surfaces, when excited with laser wavelength of 473 nm. This Raman peak is slightly shifted to 738 cm^{-1}, which is corresponded to cubic-LO phonon, when change excited wavelength to 633 nm. This result can explained by different penetration depth. It is interpreted that the GaN films exhibited more hexagonal phase in the region close to

the GaN surface region. On the other hand, the GaN films exhibited more cubic phase at the region near the GaN/GaAs interface.

Conclusions

The μ-Raman spectroscopy with the excitation wavelengths of 473, 532 and 633 nm was used as a tool to investigated crystal structures of GaN films grown on GaAs (001)- and (110)-oriented substrate surfaces. The results demonstrate that the cubic-LO phonon mode is sensitive to the excitation wavelength of 633 nm compared to other excitation wavelengths. Consequently, the laser wavelengths with different of penetration depths are also useful as a probe to excite phonons at different thickness. It is interpreted that the GaN films exhibited more hexagonal phase in the region close to the GaN surface region. While, the GaN films more dominated with cubic phase at the region near the GaN/GaAs interface. Un like GaN film on GaAs (001) substrate, by using GaAs (110) as a substrate for the growth of GaN, the film is exhibited to have a hexagonal structure as a main crystal structure associated with some cubic phase inclusion.

Acknowledgments

The authors would like to thank the 90th Anniversary of Chulalongkorn University Fund (Ratchadaphiseksomphot Endowment Fund), Ratchadaphiseksomphot Endowment Fund of Chulalongkorn University (RES5605302227-AM) for their financial support.

References

[1] S. Nakamura, T. Mukai, M. Senoh, Jpn. J. Appl. Phys. Part 2 30 (1991) L1998.

[2] I. Akasaki,H. Amano,S.Sota,H. Sakai,T. Tanaka, M.Koike, Jpn. J. Appl. Phys. 34 (1995) L1517.

[3] H. Amano, N. Sawaki, I. Akasaki, Y. Toyoda, Appl. Phys. Lett. 48 (1986) 353.

[4] S. Yoshida, S. Misawa, S. Gonda, Appl. Phys. Lett. 42 (1983) 427.

[5] Fang-Wei Lee, Wen-Cheng Ke, Chun-Hong Cheng, Bo-Wei Liao, Wei-Kuo Chen. Applied Surface Science, Volume 375, 1 July 2016, Pages 223-229

[6] Kai Wang, Yanhui Xing, Jun Han, Kangkang Zhao, Lijian Guo, Yunlong Zhang, Xuguang Deng, Yaming Fan, Baoshun Zhang. Journal of Alloys and Compounds, Volume 671, 25 June 2016, Pages 435-439

[7] Jun Wu, Fanghai Zhao, Kentaro Onabe, Yasuhiro Shiraki. Journal of Crystal Growth, Volume 221, Issues 1–4, December 2000, 276-279

[8] Sakuntam Sanorpim, , Ryuji Katayama, Kajornyod Yoodee, Kentaro Onabe, Journal of Crystal Growth 275 (2005) e1023–e1027

[9] Siripen Suandon, Sakuntam Sanorpim, Kajornyod Yoodee, Kentaro Onabe, Thin Solid Films 515 (2007) 4393–4396

Effect of Epoxy Molding Compound Floor Life to Reliability Performance for Integrated Circuit (IC) Package

U. Peanpunga [1]*, K. Ugsornrat[1], P. Thorlor[1], C. Sumithpibul[2] and A. Phoawongsa[2]

[1]Department of Industrial Physics and Medical Instrumentation, Faculty of Applied Science, King Mongkut's University of Technology North Bangkok, Bangkok, 10800

[2]Department of Engineering, UTAC Thai Limited, Bangkok, 10260

*E-mail: Udompe@utacgroup.com

Abstract

This research studied about an epoxy molding compound (EMC) floor life to reliability performance of integrated circuit (IC) package. Molding is the process for protecting the die of IC package form mechanical and chemical reaction from external environment by shaping EMC. From normal manufacturing process, the EMC is stored in the frozen at 5°C and left at around room temperature for aging time or floor life before molding process. The EMC floor life effects to its properties and reliability performance of IC package. Therefore, this work is interested in varied the floor life of EMC before molding process to analyze properties of EMC such as spiral flow length, gelation time, and viscosity. In experiment, the floor life of EMC were varied to check the effect of its property to reliability performance. The EMC floor life were varied from 0 hours to 60 hours with a step of 12 hours and observed wire sweep, incomplete EMC, and delamination inside the packages for 5x5 mm^2 of QFN packages. The evaluation showed about clearly effect of EMC floor life to IC packaging reliability. EMC floor life is not any concern for EMC property, moldabilty, and reliability from 0 hours to 48 hours for molding process of 5x5 mm^2 QFN packaging manufacturing.

Keywords: Integrated circuit (IC) packaging, Epoxy molding compound (EMC), Molding compound floor life, Gelation time

Introduction

Today, encapsulation of molding process using a transfer epoxy molding compound (EMC) is a popular method for integrated circuit (IC) packaging manufacturing. Molding is the process to protect the die in IC package form external environment for mechanical and chemical protection by shaping EMC continuing with the formation of a gelatin with complete cross linked network and leading finally to the fully cured thermoset.

EMC is thermosetting polymer which this materials with cross-linked polymer chains that has no melting temperature after they are cured. EMC is a mixture of an epoxy resin, a filler (silica, SiO_2), a hardener and other additives. The important part of EMC which is epoxy resin functions as an adhesive and binder. For silica filler part, this part is the largest portion of EMC provides excellent mechanical strength and a thermal dispersion. From normal manufacturing process, the EMC is stored in the frozen at 5°C and left at around room temperature for aging time or floor life before molding process. The EMC floor life effects to its properties and reliability performance of IC package.

Therefore, this research was interested in study to vary floor life of EMC before molding process from

0 hours to 60 hours with a step of 12 hours and analyze properties of EMC such as spiral flow length, gelation time, and viscosity. Moreover, this research also studied about molding process quality and reliability performance. The next section describes methodology of inspection effect of epoxy molding compound floor life to reliability performance for Integrated circuit package. Section 3 presents results and discussion. Finally, we conclude this paper.

Materials and Methods

This section describes about the methodology for inspection EMC property with different floor life after aging time before molding process, moldability and reliability performance were observed by using EMC on each floor life time on QFN 5x5 mm^2 package. In experiment, EMC floor life was from 0 hours to 60 hours with a step of 12 hours for analysis as shown in Table 1 and Figure 1.

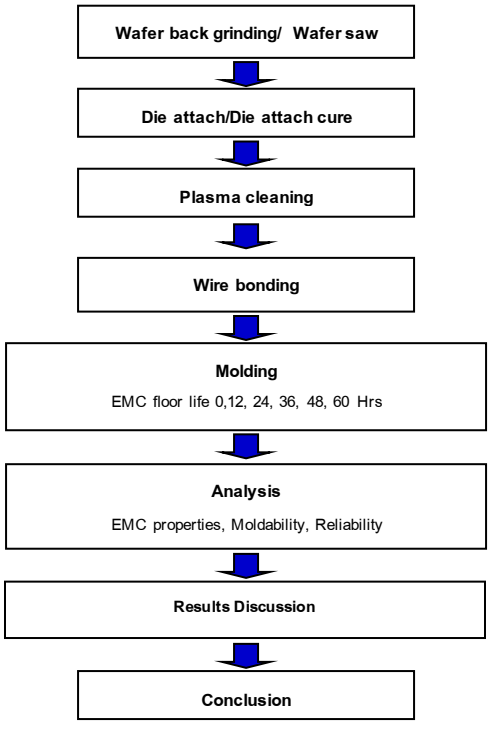

Figure 1 The experiment flow.

Table 1 Interval of EMC floor life after aging time.

Floor life (Hrs)	0	12	24	36	48	36
Compound A	1	2	3	4	5	6

For analysis, the sample was divided into three groups for inspection EMC properties consists of viscosity, gel time and spiral flow length. The second group was observed moldability with x-ray which are wire sweep and incomplete mold. The last group used for reliability testing.

For the reliability, this experiment was performed moisture sensitivity test by refer standard J-DEC-020D as shown in Figure 2, Table 2, and Table 3 (moisture/reflow sensitivity classification for nonhermetic solid state surface mount devices : MSL).

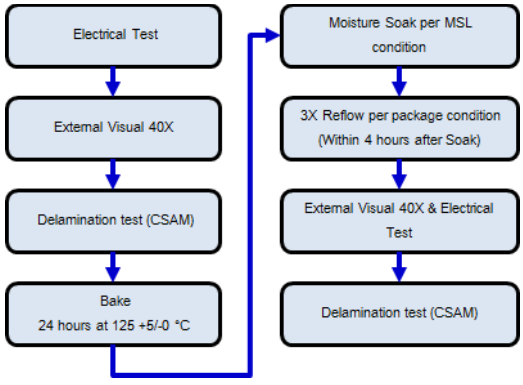

Figure 2 The procedure for moisture sensitivity level test (MSL).

Table 2 Standard of moisture sensitivity level

MSL Level	Floor life	
	Time	Condition
1	Unlimited	≤ 30 °C/ 85% RH
2	1 year	≤ 30 °C/ 60% RH
3	168 hours	≤ 30 °C/ 60% RH
4	72 hours	≤ 30 °C/ 60% RH
5	48 hours	≤ 30 °C/ 60% RH

Table 3 Standard of moisture sensitivity level for soaking requirement.

MSL Level	Soaking Requirement				
			Accelerated Equivalent		
	Standard		eV 0.40-0.48	eV 0.30-0.39	Condition
	Time (hour)	Condition	Time (hour)	Time (hour)	
1	168 +5/-0	85 °C/ 85% RH	N/A	N/A	N/A
2	168 +5/-0	85 °C/ 60% RH	N/A	N/A	N/A
3	192 +5/-0	30 °C/ 60% RH	40 +1/-0	52 +1/-0	60 °C/ 60% RH
4	96 +2/-0	30 °C/ 60% RH	20 +0.5/-0	24 +0.5/-0	60 °C/ 60% RH
5	72 +2/-0	30 °C/ 60% RH	15 +0.5/-0	20 +0.5/-0	60 °C/ 60% RH

Results and Discussion

The EMC property

For EMC properties results, spiral flow, gelation time, viscosity was determined for inspection IC package performance for 5x5 mm^2 QFN packages.

Spiral flow length

The relationship between spiral flow length test and EMC floor life is shown in Figure 3. Spiral flow is the length that EMC flow with helix shape under 1000 psi and 175 ℃. The results showed that spiral flow length was deteriorated around 20 % at EMC flow life more than 48 hours floor life. Therefore, spiral flow less than 48 hours can be acceptable for standard value of IC packaging manufacturing process.

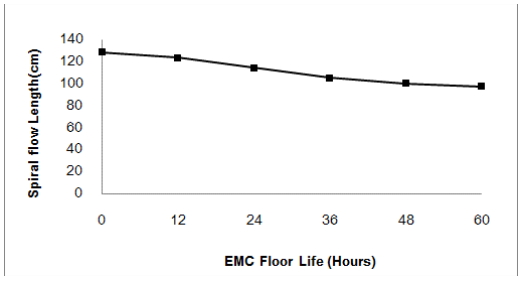

Figure 3 The relationship between spiral flow length test and EMC floor life.

Gelation time

The gelation time results are shown in Figure 4. The result shows that gelation time of EMC slightly reduce around 2% from o hours to 60 hours floor life time. The gelation time results are acceptable for IC packaging manufacturing process.

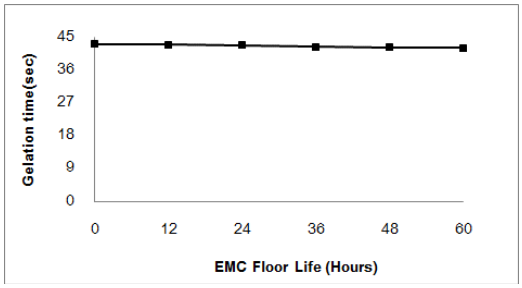

Figure 4 The gelation time for EMC floor life.

Viscosity

The viscosity results with varied EMC floor life are shown in Figure 5. The results show that gelation time of EMC slightly increase from o hours to 60 hours floor life time. The gelation time values are acceptable for IC packaging manufacturing process.

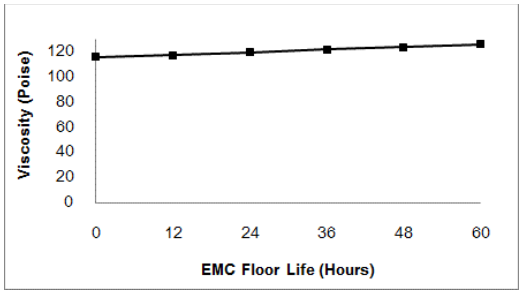

Figure 5 The viscosity results with varied EMC floor life.

Moldability

The results of wire sweep and incomplete mold used for observing moldability of 5x5 mm^2 QFN on each EMC floor life.

Wire Sweep

The wire sweep results with varied EMC floor life are shown in Table 3 and Figure 6. The wire sweep results were observed about displacement and deformation of wire loop inside the packages. The results show that wire sweep values clearly increase from o hours to 60 hours EMC floor life. For standard IC packaging manufacturing, the maximum wire sweep was controlled with 15% from standard values. However, the EMC floor life at 60 hours is closed to 15% which is maximum stand specification of wire sweep. The EMC floor life at 60 hours is acceptable or wire IC packaging manufacturing process.

Table 3 The wire sweep results for EMC floor life.

Wire sweep (%)	EMC floor life (hours)					
	0	12	24	36	48	60
Max	6.88	8.97	10.95	11.93	12.59	14.81
Min	2.04	3.39	3.18	4.66	4.28	5.32
Average	4.28	6.12	7.09	7.74	8.17	10.70

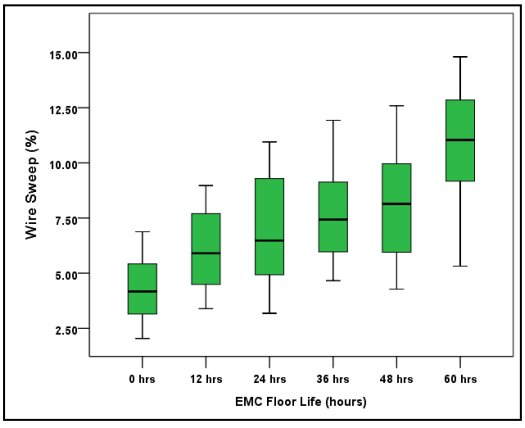

Figure 6 The wire sweep results with varied EMC floor life.

Incomplete mold

After molding process, the IC package also were observed with visual inspection to inspection incomplete molding. The inspection results show that not found incomplete mold for all EMC floor life. The result is shown in Table 4.

Table 4 The inspection results for incomplete mold of each EMC floor life

Incomplete mold	EMC Floor life (hours)					
	0	12	24	36	48	60
Result	0/760	0/760	0/760	0/760	0/760	0/760

Delamination

All IC packages were observed delamination inside the package on each EMC floor life. The results show that no any delamination, separation, and internal void for every EMC floor life as shown in Table 5.

Table 5 Delamination results for each EMC floor life.

Delamination result	EMC Floor Life (hours)					
	0	12	24	36	48	60
Result	0/760	0/760	0/760	0/760	0/760	0/760
CSAM						
TSAM						

Reliability

The IC package was tested for MSL testing with 22 units per each EMC floor life. The results show about delamination before and after testing as shown in Table 6. The results of reliability testing are acceptable for all EMC floor life due to no delamination both on die surface paddle and lead surface.

Table 6 Delamination test result before and after MSL test for EMC floor life.

Delamination result	EMC Floor Life (hours)					
	0	12	24	36	48	60
Result	0/22	0/22	0/22	0/22	0/22	0/22
Before	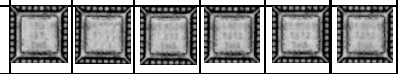					
After	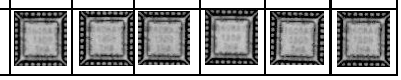					

Conclusions

This research studied about effect of epoxy molding compound floor life to EMC property,

moldability, and reliability performance QFN packages. The properties of EMC are acceptable such as gelation time and viscosity for all the floor life time spiral flow less than 48 hours can be acceptable for standard value of IC packaging manufacturing process. The mold ability also acceptable in term of wire sweep, incomplete mold, and delamination. For all EMC floor life. However, for wire sweep, the EMC floor life at 60 hours is closed to 15% which is maximum stand specification of wire sweep. For reliability test, the results show that, no delamination was observed for all packages. Therefore, EMC floor life is not any concern for EMC property, moldabilty, and reliability from 0 hour to 48 hours for molding process of IC packaging manufacturing.

Acknowledgments

This research was supported by Utac Thai Limited, Mr. Somchat Susuk and Mr. Chanwit Dulayasopaparn, employees's Utac Thai limited for recommendation and valuable comment and some data of EMC were supported from sumitomo compound supplier.

References

[1] James J. Licari (2009) "Materials and Process for electronic application". **Plastic Encapsulant Material.** Vol. 1, 47-122.

[2] N. Kinjo and Ogata (1989) "Epoxy Molding Compounds as Encapsulation Materials for Microelectronic Devices" **Raw Material for Epoxy Molding Compounds.** Vol. 88 pp 1-48

[3] Louis P. Rector Ph.D , Shaoqin Gong Ph.D. (2011) "**On the Performance of Epoxy Molding Compounds for Flip Chip Transfer Molding Encapsulation**. IEEE International Conference on Electronic Components and Technology Conference, 2001. Proceedings., 51st

[4] Peter Alpern and Kheng Chooi Lee (2008), : A Physics of Failure Approach, **"Moisture-Induced Delamination in Plastic Encapsulated Microelectronic Devices"** IEEE Trasactions on devices and materials reliability, Vol. 8 ,No.3, September 2008

[5] Chen-Hung Lee, Lu-Fu Lin (2010) "**Study on paddle delamination for quad flat no leads package**", IEEE Transactions on Microsystems Packaging Assembly and Circuits Technology Conference

[6] ASTMD3123, (1998.) American Society for test and Materials "**Standard test method for spiral flow of low pressure thermosetting molding compounds**,

[7] JEDEC J-STD-020D, "Moisture/Reflow Sensitivity /classification for Nonthematic Solid State Surface Mount Device".

Effect of Epoxy Molding Compound Floor Life to Reliability Performance for Integrated Circuit (IC) Package

U. Peanpunga [1]*, K. Ugsornrat[1], P. Thorlor[1], C. Sumithpibul[2] and A. Phoawongsa[2]

[1]Department of Industrial Physics and Medical Instrumentation, Faculty of Applied Science, King Mongkut's University of Technology North Bangkok, Bangkok, 10800

[2]Department of Engineering, UTAC Thai Limited, Bangkok, 10260

*E-mail: Udompe@utacgroup.com

Abstract

This research studied about an epoxy molding compound (EMC) floor life to reliability performance of integrated circuit (IC) package. Molding is the process for protecting the die of IC package form mechanical and chemical reaction from external environment by shaping EMC. From normal manufacturing process, the EMC is stored in the frozen at 5°C and left at around room temperature for aging time or floor life before molding process. The EMC floor life effects to its properties and reliability performance of IC package. Therefore, this work is interested in varied the floor life of EMC before molding process to analyze properties of EMC such as spiral flow length, gelation time, and viscosity. In experiment, the floor life of EMC were varied to check the effect of its property to reliability performance. The EMC floor life were varied from 0 hours to 60 hours with a step of 12 hours and observed wire sweep, incomplete EMC, and delamination inside the packages for 5x5 mm^2 of QFN packages. The evaluation showed about clearly effect of EMC floor life to IC packaging reliability. EMC floor life is not any concern for EMC property, moldabilty, and reliability from 0 hours to 48 hours for molding process of 5x5 mm^2 QFN packaging manufacturing.

Keywords: Integrated circuit (IC) packaging, Epoxy molding compound (EMC), Molding compound floor life, Gelation time

Introduction

Today, encapsulation of molding process using a transfer epoxy molding compound (EMC) is a popular method for integrated circuit (IC) packaging manufacturing. Molding is the process to protect the die in IC package form external environment for mechanical and chemical protection by shaping EMC continuing with the formation of a gelatin with complete cross linked network and leading finally to the fully cured thermoset.

EMC is thermosetting polymer which this materials with cross-linked polymer chains that has no melting temperature after they are cured. EMC is a mixture of an epoxy resin, a filler (silica, SiO_2), a hardener and other additives. The important part of EMC which is epoxy resin functions as an adhesive and binder. For silica filler part, this part is the largest portion of EMC provides excellent mechanical strength and a thermal dispersion. From normal manufacturing process, the EMC is stored in the frozen at 5°C and left at around room temperature for aging time or floor life before molding process. The EMC floor life effects to its properties and reliability performance of IC package.

Therefore, this research was interested in study to vary floor life of EMC before molding process from

0 hours to 60 hours with a step of 12 hours and analyze properties of EMC such as spiral flow length, gelation time, and viscosity. Moreover, this research also studied about molding process quality and reliability performance. The next section describes methodology of inspection effect of epoxy molding compound floor life to reliability performance for Integrated circuit package. Section 3 presents results and discussion. Finally, we conclude this paper.

Materials and Methods

This section describes about the methodology for inspection EMC property with different floor life after aging time before molding process, moldability and reliability performance were observed by using EMC on each floor life time on QFN 5x5 mm^2 package. In experiment, EMC floor life was from 0 hours to 60 hours with a step of 12 hours for analysis as shown in Table 1 and Figure 1.

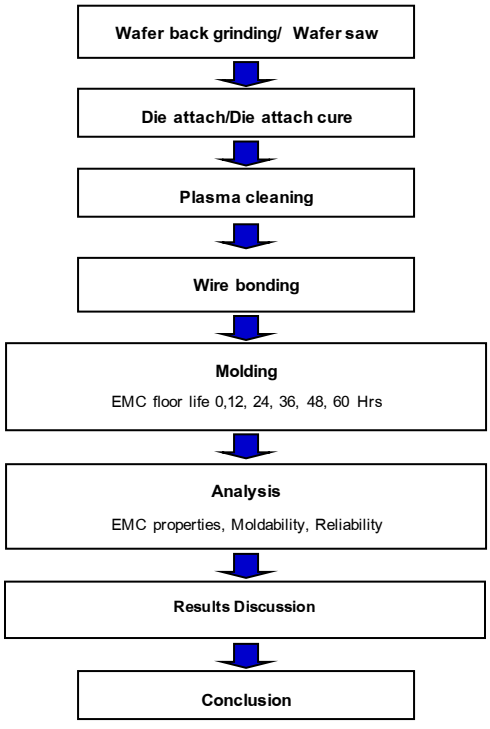

Figure 1 The experiment flow.

Table 1 Interval of EMC floor life after aging time.

Floor life (Hrs)	0	12	24	36	48	36
Compound A	1	2	3	4	5	6

For analysis, the sample was divided into three groups for inspection EMC properties consists of viscosity, gel time and spiral flow length. The second group was observed moldability with x-ray which are wire sweep and incomplete mold. The last group used for reliability testing.

For the reliability, this experiment was performed moisture sensitivity test by refer standard J-DEC-020D as shown in Figure 2, Table 2, and Table 3 (moisture/reflow sensitivity classification for nonhermetic solid state surface mount devices : MSL).

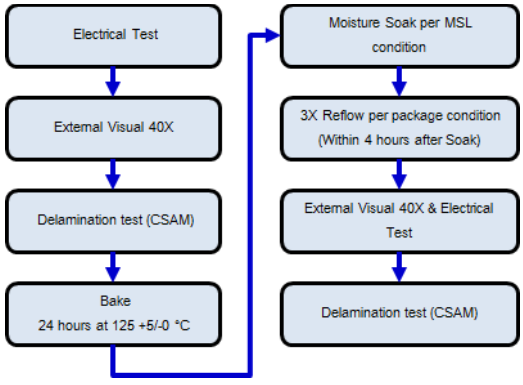

Figure 2 The procedure for moisture sensitivity level test (MSL).

Table 2 Standard of moisture sensitivity level

MSL Level	Floor life	
	Time	Condition
1	Unlimited	≤ 30 °C/ 85% RH
2	1 year	≤ 30 °C/ 60% RH
3	168 hours	≤ 30 °C/ 60% RH
4	72 hours	≤ 30 °C/ 60% RH
5	48 hours	≤ 30 °C/ 60% RH

Table 3 Standard of moisture sensitivity level for soaking requirement.

MSL Level	Soaking Requirement				
			Accelerated Equivalent		
	Standard		eV 0.40-0.48	eV 0.30-0.39	Condition
	Time (hour)	Condition	Time (hour)	Time (hour)	
1	168 +5/-0	85 °C/ 85% RH	N/A	N/A	N/A
2	168 +5/-0	85 °C/ 60% RH	N/A	N/A	N/A
3	192 +5/-0	30 °C/ 60% RH	40 +1/-0	52 +1/-0	60 °C/ 60% RH
4	96 +2/-0	30 °C/ 60% RH	20 +0.5/-0	24 +0.5/-0	60 °C/ 60% RH
5	72 +2/-0	30 °C/ 60% RH	15 +0.5/-0	20 +0.5/-0	60 °C/ 60% RH

Results and Discussion

The EMC property

For EMC properties results, spiral flow, gelation time, viscosity was determined for inspection IC package performance for 5x5 mm^2 QFN packages.

Spiral flow length

The relationship between spiral flow length test and EMC floor life is shown in Figure 3. Spiral flow is the length that EMC flow with helix shape under 1000 psi and 175 ℃. The results showed that spiral flow length was deteriorated around 20 % at EMC flow life more than 48 hours floor life. Therefore, spiral flow less than 48 hours can be acceptable for standard value of IC packaging manufacturing process.

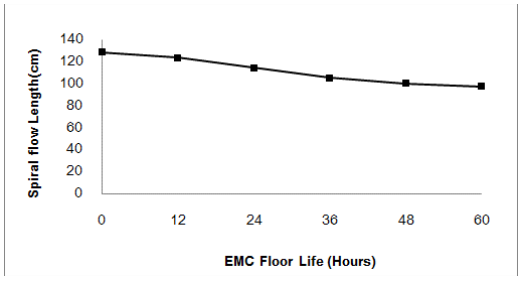

Figure 3 The relationship between spiral flow length test and EMC floor life.

Gelation time

The gelation time results are shown in Figure 4. The result shows that gelation time of EMC slightly reduce around 2% from o hours to 60 hours floor life time. The gelation time results are acceptable for IC packaging manufacturing process.

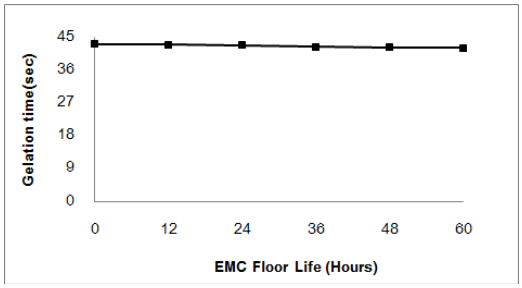

Figure 4 The gelation time for EMC floor life.

Viscosity

The viscosity results with varied EMC floor life are shown in Figure 5. The results show that gelation time of EMC slightly increase from o hours to 60 hours floor life time. The gelation time values are acceptable for IC packaging manufacturing process.

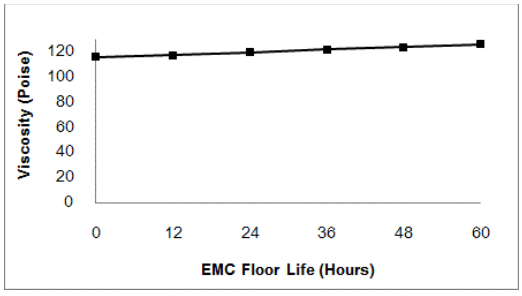

Figure 5 The viscosity results with varied EMC floor life.

Moldability

The results of wire sweep and incomplete mold used for observing moldability of 5x5 mm^2 QFN on each EMC floor life.

Wire Sweep

The wire sweep results with varied EMC floor life are shown in Table 3 and Figure 6. The wire sweep results were observed about displacement and deformation of wire loop inside the packages. The results show that wire sweep values clearly increase from o hours to 60 hours EMC floor life. For standard IC packaging manufacturing, the maximum wire sweep was controlled with 15% from standard values. However, the EMC floor life at 60 hours is closed to 15% which is maximum stand specification of wire sweep. The EMC floor life at 60 hours is acceptable or wire IC packaging manufacturing process.

Table 3 The wire sweep results for EMC floor life.

Wire sweep (%)	EMC floor life (hours)					
	0	12	24	36	48	60
Max	6.88	8.97	10.95	11.93	12.59	14.81
Min	2.04	3.39	3.18	4.66	4.28	5.32
Average	4.28	6.12	7.09	7.74	8.17	10.70

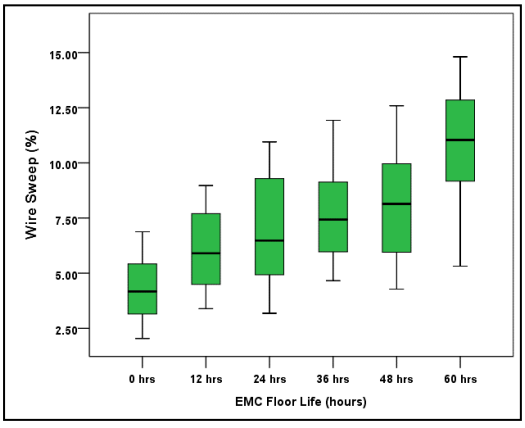

Figure 6 The wire sweep results with varied EMC floor life.

Incomplete mold

After molding process, the IC package also were observed with visual inspection to inspection incomplete molding. The inspection results show that not found incomplete mold for all EMC floor life. The result is shown in Table 4.

Table 4 The inspection results for incomplete mold of each EMC floor life

Incomplete mold	EMC Floor life (hours)					
	0	12	24	36	48	60
Result	0/760	0/760	0/760	0/760	0/760	0/760

Delamination

All IC packages were observed delamination inside the package on each EMC floor life. The results show that no any delamination, separation, and internal void for every EMC floor life as shown in Table 5.

Table 5 Delamination results for each EMC floor life.

Delamination result	EMC Floor Life (hours)					
	0	12	24	36	48	60
Result	0/760	0/760	0/760	0/760	0/760	0/760
CSAM						
TSAM						

Reliability

The IC package was tested for MSL testing with 22 units per each EMC floor life. The results show about delamination before and after testing as shown in Table 6. The results of reliability testing are acceptable for all EMC floor life due to no delamination both on die surface paddle and lead surface.

Table 6 Delamination test result before and after MSL test for EMC floor life.

Delamination result	EMC Floor Life (hours)					
	0	12	24	36	48	60
Result	0/22	0/22	0/22	0/22	0/22	0/22
Before	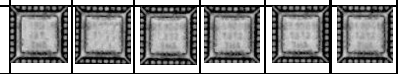					
After	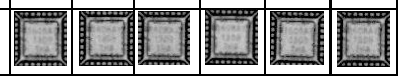					

Conclusions

This research studied about effect of epoxy molding compound floor life to EMC property,

moldability, and reliability performance QFN packages. The properties of EMC are acceptable such as gelation time and viscosity for all the floor life time spiral flow less than 48 hours can be acceptable for standard value of IC packaging manufacturing process. The mold ability also acceptable in term of wire sweep, incomplete mold, and delamination. For all EMC floor life. However, for wire sweep, the EMC floor life at 60 hours is closed to 15% which is maximum stand specification of wire sweep. For reliability test, the results show that, no delamination was observed for all packages. Therefore, EMC floor life is not any concern for EMC property, moldabilty, and reliability from 0 hour to 48 hours for molding process of IC packaging manufacturing.

Acknowledgments

This research was supported by Utac Thai Limited, Mr. Somchat Susuk and Mr. Chanwit Dulayasopaparn, employees's Utac Thai limited for recommendation and valuable comment and some data of EMC were supported from sumitomo compound supplier.

References

[1] James J. Licari (2009) "Materials and Process for electronic application". **Plastic Encapsulant Material.** Vol. 1, 47-122.

[2] N. Kinjo and Ogata (1989) "Epoxy Molding Compounds as Encapsulation Materials for Microelectronic Devices" **Raw Material for Epoxy Molding Compounds.** Vol. 88 pp 1-48

[3] Louis P. Rector Ph.D , Shaoqin Gong Ph.D. (2011) "**On the Performance of Epoxy Molding Compounds for Flip Chip Transfer Molding Encapsulation**. IEEE International Conference on Electronic Components and Technology Conference, 2001. Proceedings., 51st

[4] Peter Alpern and Kheng Chooi Lee (2008), : A Physics of Failure Approach, **"Moisture-Induced Delamination in Plastic Encapsulated Microelectronic Devices"** IEEE Trasactions on devices and materials reliability, Vol. 8 ,No.3, September 2008

[5] Chen-Hung Lee, Lu-Fu Lin (2010) "**Study on paddle delamination for quad flat no leads package**", IEEE Transactions on Microsystems Packaging Assembly and Circuits Technology Conference

[6] ASTMD3123, (1998.) American Society for test and Materials "**Standard test method for spiral flow of low pressure thermosetting molding compounds**,

[7] JEDEC J-STD-020D, "Moisture/Reflow Sensitivity /classification for Nonthematic Solid State Surface Mount Device".

Milky Way Galaxy from the Observation of 21-cm Spectral Line from HI Using SRT 4.5m of NARIT

A. Phakam[1]*, K. Asanok[1], P. Jaroenjittichai[2], P. Somboonpon[2], S. Punyawarin[2] and N. Prasert[2]

[1]Department of Physics, Faculty of Science, Khon Kaen University, 123 Moo 16 Mittapap Rd., Nai-Muang, Muang District, Khon Kaen 40002, Thailand

[2]National Astronomical Research Institute of Thailand (Public Organization), Ministry of Science and Technology, Siripanich Building, 191 Huay Kaew Road, Muang District, Chiangmai 50200, Thailand

* E-mail: p_attasit@kkumail.com

Abstract

Preliminary results are presented on the study of the kinematics of the rotation and the structure of our galaxy from observations of neutral hydrogen (HI) emission at a frequency of ~1420 MHz using a 4.5-m telescope of the National Astronomical Research Institute of Thailand. The frequency shifts resulting from the motions of HI clouds, arising from the Doppler effect, enable the calculation of the cloud radial velocities. These, in turn, can be used to obtain the rotational velocities of the clouds, from which the rotation curve of our galaxy and hence its structure and its mass distribution can be determined. The rotation curve of our galaxy is seen to be almost at with increasing distance from the center. In these measurements, HI spectra have been obtained at 5° intervals in a galactic longitude range from 25° to 85° at a galactic latitude of zero. It is assumed that the Sun is orbiting the center of our galaxy at a distance of 8.34±0.34 kpc and that its orbital velocity is 225±5 km/s.

Keywords: Milky Way, Rotation curve, Mapping the Milky Way, Neutral hydrogen

Introduction

It is difficult for astronomers to study the kinematics of our galaxy (often referred to as the Galaxy or Milky Way) because we live inside it. One of the techniques for studying the physical characteristics and rotational dynamics of our galaxy is known as the Tangential Point Method (TPM), which is ideally suited to the use of a small radio telescope. TPM and the mapping of the Galaxy using the neutral hydrogen spectral line at ~21cm wavelength are described in the next sections and finally the actual observations and results from them showing the rotation curve of the Galaxy, will be describe.

The SRT system of NARIT

The 4.5-m small radio telescope (SRT) of the National Astronomical Research Institute of Thailand has been further developed by the Thai Radio Astronomy Research Network (TRARN) group. The whole system is similar to that developed at the Haystack observatory, but the receiver system has been modified, a block diagram of which is shown in Figure 1. The output signals from the SRT, which are input into the telescope control and data collection computer and recorded, are in the form of voltages representing the signal strengths from 400 frequency channels separated in frequency by 10 kHz. This corresponds to a velocity separation of 2.107 km/s at the rest frequency of the neutral hydrogen (HI)

spectral line at ~1420.4058 MHz, arising from the hyperfine transition resulting from the interaction between the quantized nuclear spins of the proton and the electron, the receiver was configured such that its central channel corresponded to a frequency shift of +35 kHz relative to the rest frequency of the line. Thus, the 400 channels correspond to a velocity range from -414.08 to +428.87 km/s.

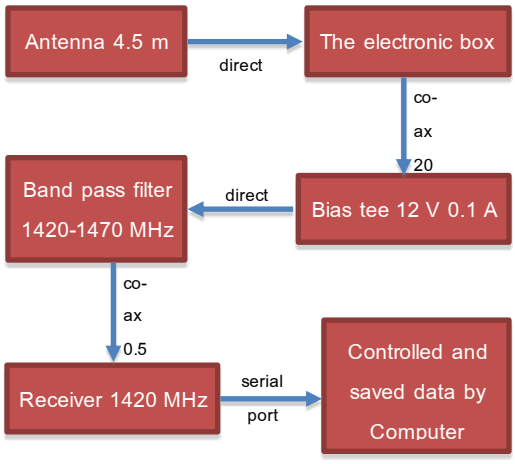

Figure 1 The system of SRT from NARIT, the electronic box are composed of 2 LNA, Bias tee and Band pass filter 1420-1470 MHz.

Tangential point method (TPM)

This topic explains how to find the rotation curve of Milky Way Galaxy. The data from SRT are calculated line-of-sight velocities (or called radial velocities) from Doppler shift effects which are used in tangential point method (TPM). TPM diagram can be explained as shown in Figure 2. The line-of-sight velocity at tangential point in quadrant I and quadrant IV is maximum velocity from blueshift effect and minimum velocity from redshift effect respectively which those velocities are called the terminal velocity (V_T). We use V_T to calculate the rotational velocity (in term of V) as shown in Equation (1) and Equation (2) and the galactic distance (in term of R) can be calculated using Equation (3) which R_0, V_0 and l are galactic distance of Solar system, the rotational velocity of Solar system and galactic longitude respectively. Rotation curve is plotted between the rotational velocities and galactic distances.

$$V = V_{T,Max} + V_0 \sin l \; ; l > 0° \quad (1)$$

$$V = V_{T,Min} + V_0 \sin l \; ; l < 0° \quad (2)$$

$$R = R_0 \sin l \quad (3)$$

Materials and Methods

Mapping the Milky Way galaxy

However, mapping our galaxy will give us to understand the physical properties and its morphologies. In each galactic longitude have many line-of-sight velocities which all those velocities will be calculated as the position of HI in our galaxy using Eq.4 whereas $v_{l\text{-}o\text{-}s}$ is line-of-sight velocity. Plotting between galactic distance and galactic longitude in polar coordinate system is used to map the distribution of HI in Milky Way galaxy.

$$R = (R_0 V_0 \sin l) / (V_0 \sin l + V_{l\text{-}o\text{-}s}) \quad (4)$$

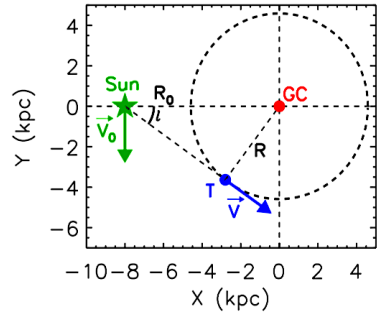

Figure 2 Illustration of tangential point: Sun, Galactic Center (GC), tangent-point (T) assumed by the tangential point method (Renaud et al. 2013).

Results and Discussions

Scope of the study, HI spectrum is observed at galactic latitude 0° and from galactic longitude 25° to 85° with increasing 5° in each step. The parameters are used in this calculation as follows; the rotational velocity of Solar system is equal to 225±5 km/s and

galactic distance of Solar system is equal to 8.34±0.34 kpc respectively. Figure 3 shows rotation curve of Milky Way galaxy from TPM. Moreover, TPM has limitation for calculating especially the distance outer of Solar system because the galactic distance can be calculated maximum at R_0 as shown in Equation (3). The dish sizes of radio telescope and tracking system have effect for measuring the position of source also.

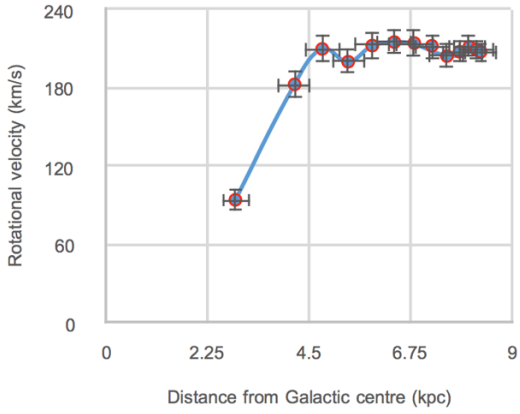

Figure 3 Rotation curve of our galaxy obtained from SRT observation.

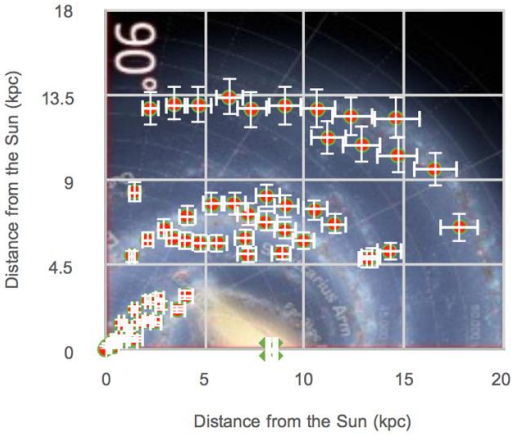

Figure 4 The comparison between HI's map from SRT and schematic of the Milky Way by R. Hurt (SCC-Caltech).

In Figure 4 shows HI's map of our Galaxy which the dots and error bars denote the positions of HI in Milky Way in each galactic longitude, the yellow line represents scope of the study, the green cross and error are the position of galactic center and start point is the Solar system's position. The error bars of HI's positions are increased when the Galactic distance is increasing. The distributions of HI in the map are well compatible with the arm of our galaxy especial in the first quadrant. When we compare between the HI' map from SRT and schematic of the Milky Way by R. Hurt (SCC-Caltech).

Conclusions

The rotation curve of our galaxy is almost flat showing constant velocity with increasing distance from the Galactic center which contradicts the Kepler's law. The result reveals that total mass within the Milky Way galaxy increases nearly constantly with increasing galactic radius. The distribution of HI's in the map is similar to the arm structure in schematic of Milky Way galaxy obtained from R. Hurt (SCC-Caltech) which represents reliability results of 4.5m SRT. However, SRT of NARIT has some limitation for observation which it cannot observe the elevation of celestial sphere objects below 25° because this observation will affect to balance of SRT and will be damaged for SRT. Moreover, the line-of-sight velocities are observed at galactic longitude with increasing 5° in each step which is big size step and effect to reliability of data. Therefore, we will re-observe at galactic longitude with increasing 3° in each step which the step sized is equal to beam size of SRT from NARIT. Therefore, we will re-observe at galactic longitude with increasing 2° to 3° in each step which the step sized should be equal to less than the beam size of SRT from NARIT for which to proof the telescope accuracy.

Acknowledgments

Department of Physics, Faculty of Science, Khon Kaen University Development and Promotion of Science and Technology Talents (DPST) Thai Radio Astronomy Research Network (TRARN)

References

[1] Burton, W.B., in Galactic and Extragalactic Radio Astronomy, 1988, verschuur G.L.,Keller-Mann, K.I. (editors), Springer-Verlag

[2] Horellou C. and Johansson D. *Hand-On Radio* Astronomy Mapping the Milky Way.

[3] Renaud, F., et al. (2013). *MNRAS, 436*, 1836;

[4] Yoshiaki S. The Mass Distribution and Rotation Curve in the Galaxy.

[5] The HI 21 cm Line, www.cv.nrao.edu/course/astr534/HILine.html", retrieved on 29 Nov., 2015.

[6] Hurt R. Schematic of the Milky Way, apod.nasa.gov/apod/ap080606.html, retrieved on 18 Jan., 2016.

Photometric Monitoring of Active Galactic Nuclei for Short-term Variability

S. Charoensiri[1*], M. Shramm[2] and W. Rujopakarn[1]

[1]Department of Physics, Faculty of Science, Chulalongkorn University, 254 Phyathai Road, Patumwan, 10330, Thailand

[2]National Institute of Advanced Industrial Science and Technology Tsukuba-central 3-1, Umezono 1-1-1, Tsukuba, Ibaraki 305-8563, JAPAN

*E-mail: supharatjc@gmail.com

Abstract

Active Galactic Nuclei (AGNs) typically show variability on all time scales which can range from days to years. The purpose of this work is to study intra-year variability (i.e., month-timescale) of AGNs through photometric monitoring in order to determine candidates for a follow-up study for reverberation mapping techniques. Our sample of AGNs are drawn from a well-defined quasar sample from the Hamburg/ESO Survey or HES, which consists of 330 quasars with redshifts $z < 0.3$. We have used the robotic Thai Southern Hemisphere Telescope at Cerro Tololo Inter-American Observatory in Chile to observe the targets in optical broadband B, V and R filters. After standard image calibration, we use a custom-written pipeline based on publicly available software to produce light curves from our observation for future analysis. We analyze the light curves to determine whether the target quasar shows intra-year variability and compare our photometry with the original HES data which was taken about 25 years ago to further study decade-scale variability. Here, we present our current results of our light-curve analysis and show some particularly notable example, such as HE1309-2501 with significant variability over short timescales.

Keywords: Active Galactic Nuclei, Intra-year variability, Photometric monitoring, Reverberation mapping

Introduction

After astronomers have discovered the existence of Supermassive black hole (SMBH) at the center of galaxies in the universe including the Milky Way and have also found its correlation with the bulge of the galaxy (M-Sigma relation). *Active Galactic Nuclei or AGNs* were later identified and known as the phenomena that occur when matter falls onto the Supermassive Black Hole (SMBH) causing its accretion disk to release a large amount of energy or outburst; therefore, astronomers have questioned and started to find out that *"What are its processes and mechanism? How are its structures? How does the M-sigma relation affect the galaxy evolution?"* by estimating the SMBH mass through the AGN's structure called the broad-line region (BLR) and the variability of the AGN when it outbursts with reverberation mapping technique, which is a primary method for black hole mass.

However, it is a spectroscopic technique which requires long-time exposures at a telescope measuring spectra of the selected targets, hence, Photometric monitoring technique is frequently used to solve this problem.

We already know that AGNs show variability on all time-scales ranging from minutes to years, in other

words, we might find AGNs that have short-term variability. Nevertheless, the researches in the short-term variability of AGNs have not been thoroughly studied. The main purpose of this project is to study the intra-year variability (i.e., month-timescale) of a set of 330 well-defined quasars drawn from the HES catalog systematically by using the robotic Thai Southern Hemisphere Telescope at Cerro Tololo Inter-American Observatory in Chile through the photometric monitoring in order to primarily identify whether the AGNs have short-term variability for further study by reverberation mapping techniques with our Python script pipeline based on publicly available software which is a general software specifically written to calculate magnitudes and produce light curves from our sample observations for data analysis and compare our photometry with the original data observed 20-25 years ago.

Materials and Methods

As mentioned in the previous section, photometric monitoring is a major technique applied in this project to detect whether our sample objects show any outburst, thus, monitoring is performed in three optical broadband filters.

We then calculate the magnitude and estimate the target light curve with absolute photometry.

However, since our absolute photometry poorly calibrates our target by using the reference star catalog e.g. UCAC4 (Zacharias et al, 2012) we are looking forward to use relative photometry in our analysis which is independent of systematic errors from Zero-point calculation.

In addition, relative photometry is used to correct the measurement error due to the sensitivity of the atmospheric variation in each night along the observation and also due to the instrument itself by using the PROMPT8 Telescope with our written algorithm sets for further data analysis.

However, we also calibrate our fields to either SDSS photometry or UCAC4 catalog in order to study long-term variability compared with the data 25 years ago and then to calibrate spectroscopic follow-up observation.

The Sample and Reference Catalogues

Our AGN targets are well-defined quasars (Wisotzki, 2000) from the Hamburg/ESO Survey (HES) operated by the University of Hamburg and the European Southern Observatory (ESO) since 1990. The survey is taken with the 1-m ESO Schmidt telescope and the 4-degree prism at La Silla observatory. In this catalog contains statistic data of stars, galaxies and also quasars whose magnitude range of $13 < Bj < 18$. This survey has many purposes such as studying and making a catalog of low-redshift quasars and the most luminous quasars with high redshifts $1.5<z<3.2$, etc. The survey area consists of 380 fields or around 9500 square degrees which is covered all the total southern extragalactic sky.

Another catalog used in this project is the fourth United States Naval Observatory (USNO) CCD Astrograph Catalog or UCAC4. This catalog was managed by the U.S. Naval observatory (USNO) under the UCAC project since 1998 and it was released to the public in 2012. The UCAC4 is one of the catalogs in Cerro Tololo Inter-American Observatory (CTIO) in Chile and contains over 113 million objects. Each of which also shows statistic data in a text file (ASCII file), for example, the position, magnitude and flux of the objects in B, V, g, r and I filters.

Moreover, it also contains data of the stars whose magnitudes are 8 to 16. Users can download the object data from the website http://vizier.u-strasbg.fr/viz-bin/VizieR by identifying its positions, i.e., right ascension (RA) and declination (DEC).

Thus, this project is to study, particularly in a set of 330 bright quasars drawn from the HES catalog with low redshifts of $0 < z < 0.3$ and we also use the stars drawn from the UACA4 catalog which have

magnitudes less than 18 as the reference stars in order to calculate the zero point for absolute photometry calculation of AGNs.

The PROMPT8 Telescope

To detect the outburst of our sample, we use the robotic Thai Southern Telescope in Cerro Tololo Inter-American Observatory in Chile called "PROPMT8", which is a 0.6-m telescope and one of the six telescopes under the Panchromatic Robotic Optical Monitoring and Polarimetry Telescope (PROMPT) project operated by the University of North Carolina (UNC) in association with National Astronomical Research of Thailand (NARIT).

Users can remotely use the PROMPT8 telescope and download data via Skynet system. The images of the object will be automatically calibrated to reduce some noise from the telescope itself. The data we get from the Skynet is in the form of FITS file, thus, it's ready to be used for further astronomical analysis.

The Algorithms and Data Analysis

After we use the telescope to take many exposures of the interested objects via the Skynet system. We will have an imported folder of the FITS images combining all observed images together for each observation night. These images will be partially calibrated and still have noise.

Python script pipelines based on publicly available SWARP and SExtractor have been written and developed in order to perform our absolute photometry and produce light curves of the objects for AGN variability analysis. (Vijarnwannaluk, 2015)

First, we have to run the first checker program to categorize the observed images which may consist of the images in B, V, R or other filters and primarily remove bad frames.

We then use our custom-written pipelines which have three algorithms to perform photometry and analyze the data by following these four steps.

Step 1: Run the first algorithm to align the positions and stack the images of each night in order to increase signal-to-noise ratio using Swarp. It then will select only the stacking image that has its signal-to-noise ratio more than 12. After that SExtractor will extract all statistic data of all objects in the image into a text file containing, for example, a list of the objects, the flux and error of the objects, etc. Next, it will check whether there is the AGN appeared in the image or not. Consequently, we will have the statistic values text file i.e. the start and end time of any observation, cadence, filter type, observation ID, a number of good images and a total number of the images.

Step 2: Run the second algorithm to calculate the zero point of the selected reference stars and error in the image for each night from the UCAC4 catalog. This algorithm will test whether each of all the stars in each image has its magnitude range less than 25, its ellipticity range more than 0.3, its distance from the object range more than 3 arcsec and its full width half maximum (FWHM) in a range of 0.003 to 0.03 or not. We then get a text file containing zero point and its error values using the sigma-clipping technique.

Step 3: Run the last algorithm to perform the absolute photometry for variability analysis and then calculate the magnitude and error of the object in which can be calculated from the zero point text file of the reference stars from the second algorithm and the flux text files of the objects extracted by SExtractor in the first algorithm. It then generate the light curves of our objects in B, V and R filters and also the zero point of all reference stars in each night.

Finally, we will have a result text file containing the observed day (MJD), the zero point and the error of the reference stars in each night, and the magnitude and the error of our object.

Step 4: Recheck the data in each light curve whether our magnitude results have the typical error values in our limit range or not. It should not be more than 0.10. If so, we have to check the data, sort that

bad frame out of the good ones and then run all the algorithms to produce the light curve again.

Results and Discussion

As we have applied our Python pipelines to perform photometry, calculate the magnitude and error, and produce light curves with our current sample set of 35 objects from a total of 330 quasars from the Hamburg/ESO Survey (HES) catalog. However, this is only the current state of our analysis. We already have the obtained data for more than 100 AGNs which are awaited for further analysis.

Short-Term Variability Detection

In this section, we show some of our analyzed results in a form of statistic tables and light curves, which have changed their magnitude in different variability amplitudes and time-scales as shown in Table 1 and Figures 1-6.

Table 1 Statistic data of HE1106-2301 in B, V and R filters, where HES magnitude: Bj = 15.04 or B=15.22.

HE1106-2321	B	V	R
Night (day)	74	-	-
Cadence (day)	1.8	-	-
Min mag	14.56	-	-
Max mag	15.43	-	-
Median mag	15.06	-	-
Typical mag error	0.03	-	-
Variability amplitude	0.88	-	-
Mag difference from HES (B)	-0.16	-	-

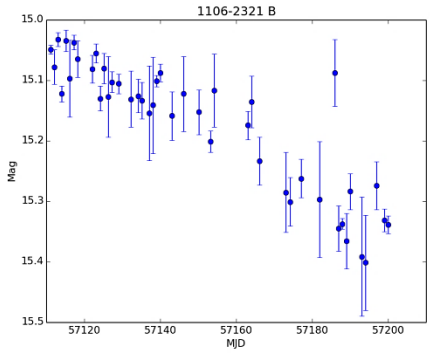

Figure 1 Short-term variability light curve of HE1106-2321 in B filter.

As shown in Figure 1, HE1106-2321 in B filter observed over 74 nights or around 2 months with a redshift of 0.086 and its average cadence of 1.8 days.

We clearly see a magnitude change in each filter. In B filter as there is a steady drop in magnitude since 57111 until 57200 MJD, which shows strong variability over month-timescales with the significant variability amplitude of 0.88. Thus, the object has its Johnson magnitude of 17.06 with the typical error bars of 0.04 in B filter. Nevertheless, we need more completed observation data in B, V and R filters to confirm whether the variability of the object in each filter is correlated.

This object also tends to have very small long-term variability as there was a small rise about 0.16 in the Johnson B-band magnitude in comparison with the HES data.

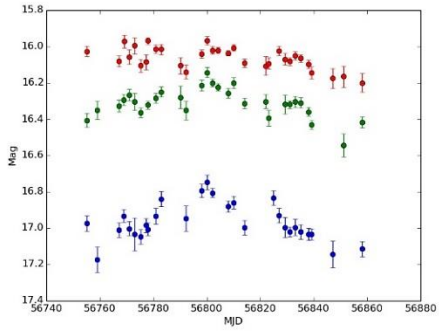

Figure 2 Short-term variability light curve of HE1309-2501 in three optical broadband.

Table 2 Statistic data of HE1309-2501 in B, V and R filters, where HES magnitudes: Bj = 17.11 or B = 17.42

HE1309-2501	B	V	R
Night (day)	28	29	31
Cadence (day)	3.5	3.1	3.1
Min mag	16.75	16.14	15.97
Max mag	17.17	16.54	16.20
Median mag	17.00	16.31	16.06
Typical mag error	0.04	0.03	0.03
Variability amplitude	0.43	0.40	0.23
Mag difference from HES (B)	-0.42	-	-

Figure 2 shows the light curve of HE1309-2501 observed over 61 nights or around 2 months with a redshift of 0.062 and its average cadence of 3.2 days.

In B filter, its magnitude has increased dramatically starting from 56755 MJD. After that it has reached a peak at 56800 MJD and finally decreased in its magnitude significantly. Hence, we can clearly see that this object shows variability in each filter over month timescales as there is strong variability in B filter with the amplitude of 0.43 and followed by V filter with the amplitude of 0.40; whereas, there is almost no change in magnitude in R filter with the smallest amplitude of 0.23.

Consequently, its Johnson magnitudes in B, V and R filter are 17.00 with the typical error of 0.04, 16.30 with the typical error of 0.03 and 16.06 with the typical error of 0.03, respectively.

Furthermore, this object tends to have very small long-term variability at this current state since the B magnitude of the object compared with the data observed about 25 years ago in B filter slightly dropped around 0.42.

Table 3 Statistic data of HE1348-1758 in B, V and R filters, where HES magnitudes: Bj = 15.77 or B = 16.10.

HE1348-1758	B	V	R
Night (day)	97	100	92
Cadence (day)	1.6	1.5	1.7
Min mag	15.59	14.80	14.26
Max mag	15.96	15.06	14.67
Median mag	15.76	14.93	14.54
Typical mag error	0.03	0.03	0.03
Variability amplitude	0.37	0.26	0.32
Mag difference from HES (B)	-0.38	-	-

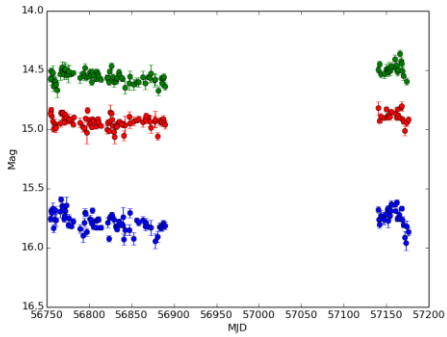

Figure 3 Short-term variability light curve of HE1348-1758 in three optical broadband.

Figure 3 shows the light curve of HE1348-1758 observed over 289 nights or around 9 months with its redshift of 0.014 and average cadence of 1.6 days.

This object almost shows no variability as its magnitude steadily fluctuates in V and R filters from 56750 to 56900. Yet we can still see some variability in month scales in B filter. Moreover, we can also see the magnitude change again as there is a moderate rise in each filter at MJD 57140 and then there is a sharp drop at MJD 57150, which is clearly seen in B filter with amplitude of 0.37. Thus, its Johnson median magnitudes in B, V and R filter are 15.76, 14.93 and 14.54 with their average typical errors of 0.03, respectively.

However, this object tends to have a gradual fall in long-term variability about 0.38 in the Johnson B-band magnitude in comparison with the HES data.

Table 4 Statistic data of HE1353-1917 in B, V and R filters, where HES magnitudes: Bj = 17.30 or B = 18.07.

HE1353-1917	B	V	R
Night (day)	53	52	53
Cadence (day)	1.45	1.42	1.37
Min magnitude	16.10	15.17	14.66
Max magnitude	16.45	15.23	15.03
Median magnitude	16.30	15.30	14.80
Typical error	0.03	0.02	0.03
Variability amplitude	0.35	0.31	0.37
Mag difference from HES (B)	-1.77	-	-

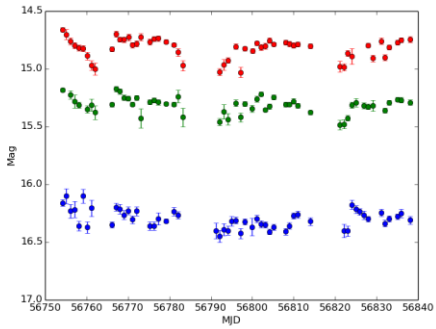

Figure 4 Short-term variability light curve of HE1353-1917 in three optical broadband.

Figure 4 shows the light curve of HE1353-1917 observed over 158 nights or around 5 months with a redshift of 0.034 and its average cadence of 1.4 days.

This object shows variability over week and month timescales in all three broadband. There was a strong change over week timescales in Johnson magnitude mostly seen in R filter as there was a sharp fall in magnitude since MJD 56752 until MJD 56760, and then the magnitude began to rise and considerately fall again over two week at MJD 56775.

Similarly, the variability in B and V filters were also in the same trends, but it has smaller variability amplitudes. Therefore, its Johnson magnitude in B, V and R filters are 16.30, 15.30 and 14.80 respectively, with the average typical errors around 0.03.

We can also see some significant trend of the long-term variability in this object as there was a very big fall in Johnson B-band magnitude about 1.77 in comparison with the HES data, which is relatively significant.

Table 5 Statistic data of HE1417-0909 in B, V and R filters, where HES magnitudes: Bj=17.19 or B=17.67.

HE1417-0909	B	V	R
Night (day)	67	59	61
Cadence (day)	1.8	1.8	1.8
Min magnitude	16.60	15.75	15.75
Max magnitude	17.42	16.15	16.04
Median magnitude	16.87	15.96	15.89
Typical error	0.03	0.04	0.04
Variability amplitude	0.81	0.40	0.29
Mag difference from HES (B)	-0.80	-	-

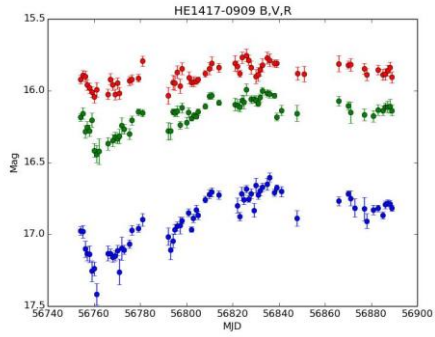

Figure 5 Short-term variability light curve of HE1417-0909 in three optical broadband.

Figure 5 shows the light curve of HE1417-0909 observed over 187 nights or around 6 months with a redshift of 0.044 and its average cadence is less than 1.8 days. It can be seen that there are similar trends in all filters. Yet we can clearly see strong variability in

R filter as the magnitude has a sharp fall with an amplitude of 0.5. Then, it has a dramatic increase in magnitude at MJD 56760 and reached a peak around MJD 56835 with amplitude around 0.9.

Finally, its Johnson magnitude in B, V and R filters are 16.87, 15.96 and 15.89 respectively with the typical errors around 0.03-0.04.

Likewise, this object tends to show long-term variability as there was a fall in Johnson B-band magnitude about 0.8 in comparison with the HES data, which is somewhat significant.

Table 6 Statistic data of HE2302-0857 in B filter, where HES magnitude: Bj=16.40 or B=16.58.

HE2302-0857	B	V	R
Night (day)	24	-	-
Cadence (day)	1.6	-	-
Min magnitude	15.04	-	-
Max magnitude	15.67	-	--
Median magnitude	15.28	-	-
Typical error	0.03	-	-
Variability amplitude	0.63	-	-
Mag difference from HES (B)	-1.30	-	

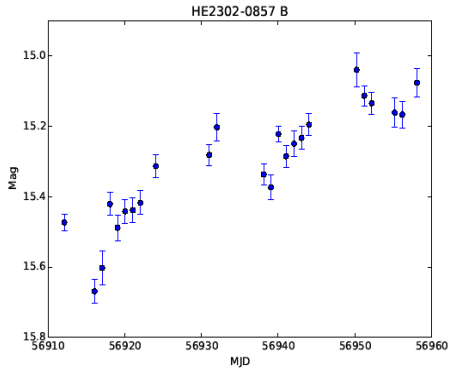

Figure 6 Short-term variability light curve of HE2302-0857 in B filter.

Figure 6 shows the light curve of HE2302-0857 observed over 24 nights or around three weeks only in Johnson B filter with a redshift of 0.046 and its average cadence of 1.6 days.

This object shows variability over week timescales as there was a dramatic change in Johnson B-band magnitude starting from MJD 556915 until MJD 56959. Nevertheless, more observed data in V and R filters are required in order to see if it has related variability in B filter.

It also tends to show long-term variability as there was a big decline in Johnson B-band magnitude around 1.3 in comparison with the HES data, which is relatively significant.

Long-Term Variability Trend

In this section, we represent the bar graph showing the difference in Johnson B-band magnitudes of our example candidates and full sample compared with HES data observed about 20 years ago to see whether our targets has any long-term variability trend as shown in Figure 7.

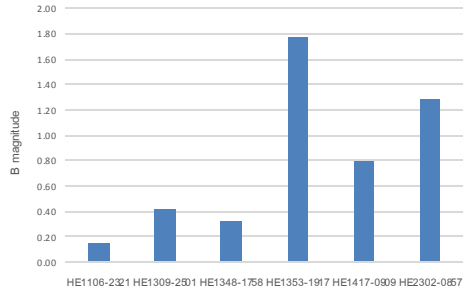

Figure 7 The bar graph showing the difference in B-band magnitude between six examples and HES data.

It can be seen from Figure 7 that HE1353-1917 has the strongest long-term variability with Johnson B-band magnitude of 1.77. Second and third are HE2302-0857 and HE1417-0909 whose Johnson B-band magnitudes are 1.29 and 0.80 0.43 respectively.

The three remaining objects are HE1309-2501 and HE1349-1758 with the B-band magnitude of 0.43, 0.33 and 0.15 respectively.

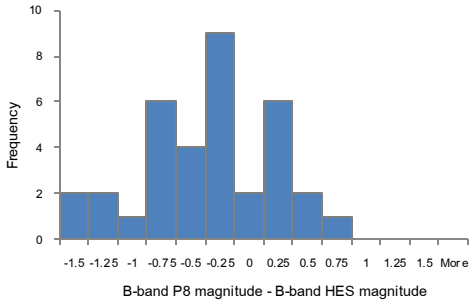

Figure 8 The histogram showing the difference in B-band magnitude between our full sample and HES data.

Figure 8 shows the distribution of B-band magnitude difference between our full sample and HES data. There are 30 objects that shows short-term variability in B-band magnitude with its range less than 0.75. We can also see that there are 5 objects as its B-band magnitude significantly decreased with a range more than 1.0 which tend to show strong long-term variability.

AGN Luminosity and Its Variability Amplitude

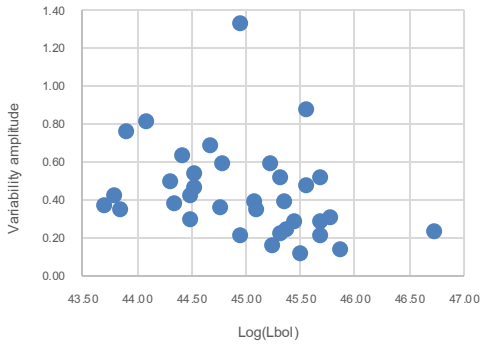

Figure 9 The graph representing the AGN luminosity from HES catalog in logarithm scale (x-axis) and AGN variability amplitude from our 36 candidates in B band (y-axis).

In this section, we consider the AGN luminosity and variability amplitude relation in B, V and R band as Figure 9 showing an example plot in B band. We can see similar trends in each band; the lower the AGN luminosity is, the stronger the variability becomes.

As the AGN bolometric luminosity is proportional to the black hole mass and related with the Eddington ratio and the growth of black hole mass is very small over the timescale, which is constant.

Therefore, the Eddington ratio is then dominated by bolometric luminosity (Lbol) term which is defined by the AGN continuum luminosity. In other words, if there is currently a strong change in AGN continuum luminosity and the black hole mass is assumed to be constant.

Thus, the Eddington ratio might change quite dramatically about 0.2-0.3 dex as most of our sample variability appeared to have a Johnson B-band magnitude change ranging from 0.6-0.8.

Conclusions

After we study the short-term variability of AGNs from the HES catalog by using the robotic Thai Southern telescope (PROMPT8) to monitor the outbursts of our 35 candidates and then perform photometry and produce their light curves for a further study for reverberation mapping technique by our custom-written pipelines, which is consistent, effective and available to analyze other candidates with the magnitude uncertainty less than 0.1.

We found that our objects have variability over different amplitudes with the amplitude range less than 1.0 e.g. HE1309-2501 and over various timescales ranging from days, weeks or months with their average typical errors less than 0.05.

We also found some objects that have trends of long-term variability assumed from the difference in B-band magnitude of our sample and the HES data with a magnitude range less than 1.8.

The magnitude errors might be affected from the atmospheric variation or other factors during the observation for each night such as strong wind, bad weather, telescope maintenance, unknown gradient, etc.

We have to continue monitoring the outbursts of our targets for more precise and accurate analysis. Hence, we are ongoing to analyze the variability of more than 100 candidates.

Acknowledgments

We would like first to thank NARIT and the University of North Carolina for creating the PROMPT telescope program. Next, we would like to specially thank Chulalongkorn Univeristy, Dr.Malte Shramm and Dr.Wiphu Rujopakarn for their supports and contribution in this project.

References

[1] Graham et al. A possible close supermassive black-hole binary in a quasar with optical periodicity. [Online]. 2015. Available from: http://arxiv.org/pdf/1501.01375v1.pdf [2016, January 29]

[2] Vijarnwannaluk, Bovornpratch., Schramm, Malte., and Rujopakarn, Wiphu. Photometric monitoring of active galactic nuclei using the Thai Robotic Telescope in Chile.n.p., 2015.

[3] Schneider,Peter. An Introduction to Extragalactic Astronomy and Cosmology.Springer-Verlag, Berlin, Heidelberg, 2006.

An Optical Diagnostic Technique for Laser Removal of Graffiti

J. Rattanarojpan1[1,2*], P. Kittiboonanan[2], S. Sriboonsong[1] and A. Ratanavis[1,2]

[1]Department of Industrial Physics and Medical Instrumentation, Faculty of Applied Science, [2]Lasers and Optics Research Center (LANDOS), Science and Technology Institute. King Mongkut's University of Technology North Bangkok, Bangkok, Thailand

*E-mail: jidako22@gmail.com

Abstract

In this paper, we propose an optical surface measurement based on laser scattering to monitor situ the laser cleaning threshold for the removal of graffiti. This technique is meant to assist the laser removal process using laser pulses of 10 ns at 1064 nm while probing the weak laser beam at 632 nm. The diagnostic apparatus consists of a He-Ne laser performing a probing light source and photodiodes. A polarizing beam splitting cube is used to split the probe beam into two separate beams which are called the reference beam and the sample beam. The reference beam is sent to the unaffected graffiti surface while the sample beam is incident on the affected graffiti surface. The spots of the two probe beams on the surfaces are imaged onto photodiodes. In this approach, the signals detected by photodiodes can be analyzed and indicated the laser cleaning threshold. A setup of angular laser cleaning allows the simplicity of this optical measurement. For this study, the use of a Q-switch Nd:YAG laser operating at 1 Hz was investigated. By mean of the Z-scan method, the laser fluence of the laser cleaning beam can be varied. The sample under investigation is irradiated by the Z-scan laser beam achieved by the scanning lens. The level of laser cleaning has been also determined through the optical setup. The laser removal of graffiti from mortars under dry and wet conditions was attempted to examine the cleaning procedures. The results obtained by this demonstration have proven to be a reliable technique for an online surface inspection for laser cleaning applications. Furthermore, this optical diagnostic technique can allow a variety of interesting applications for laser cleaning technology.

Keywords: Laser cleaning, Angular laser cleaning, Online surface inspection

Introduction

Graffiti can be defined as undesirable markings on value objects, heritage sites, public places and natural features [1,2]. In Thailand, graffiti is now seriously concerned as uninvited markings that spoil original values of Thai cultural heritage. At the same time, graffiti can be now respected as public arts. The views of graffiti can be different depending on the situations, places and permission.

However, the removal of distracting graffiti can be regarded as the final solution to eliminate unwanted markings. There are several methods of the graffiti removal such as water jet, grit-blasting and chemical approaches etc. In case of mortar surfaces, these methods can result the damage of underlying surfaces. The use of these methods has to be carefully accounted as the appropriate and appreciate directions to conserve the original values of the cleaning surfaces. In traditional ways, the chemical

removal seems to be a good candidate for the graffiti removal. However, it suffers for the danger to health and uncontrollable reaction to the cleaning surface. In addition, the chemicals used in graffiti removal can leave the chemical remains or stains on the surface [2,3].

To overcome these problems, lasers has been introduced as an alternative method for the graffiti removal. Laser cleaning technique offers the selective control area and non-contact action. Despite of successes, there is still room for further developments. The investigation of the cleaning fluence during cleaning procedures is still meant to be a challenge. The online inspection can indicate the suitable laser parameters such as energy density, wavelength, pulse duration and pulse repetition rate of the laser. It can diminish the damage occurred by the laser [4-11].

In very recent years, an online inspection based on laser scatting has been developed [12]. The image processing has been used to determine the cleaning threshold [12]. To support this activity, we propose an optical diagnostic technique of the graffiti removal by using Nd:YAG laser equipped with an online inspection. This work aims to combine of the angular laser cleaning and Z-scan method to remove graffiti from mortars under dry and wet conditions. This invention offers the marriage of the principle of laser scattering and light detection provided by very fast photodiodes that allow the optical inspection during the laser cleaning process. This diagnostic setup can be applicable to the practical cleaning procedures on devastating sites caused by graffiti.

Materials and Methods

As mentioned previously, this technique composes of the angular laser and Z-scan methods.

Figure 1 shows the schematic diagram of the setup. The painted mortars shown in Figure 2 are assumed as the samples affected by graffiti. The diagnostic apparatus consists of the He-Ne laser beam served as a light source and photodiodes. The He-Ne laser beam at the wavelength of 632 nm performs as the probe beam. By using polarizing beamsplitter, the probe beam is split up into two separate beams which are called the reference beam and the sample beam. As consequences, the reference beam is directed onto the unaffected graffiti sample while the sample beam is sent to the affected graffiti sample. The spots of the two probe beams on the two samples are simultaneously imaged onto photodiodes. Signals observed from photodiodes are compared to indicate optimal parameters for the laser cleaning.

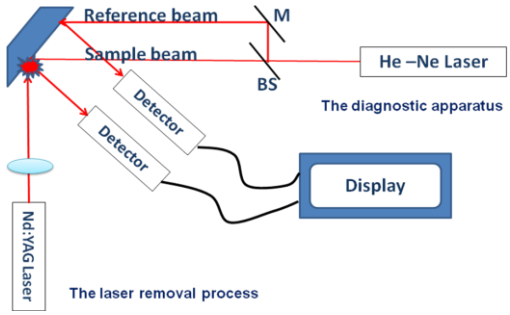

Figure 1 A simplified diagram of the experimental setup.

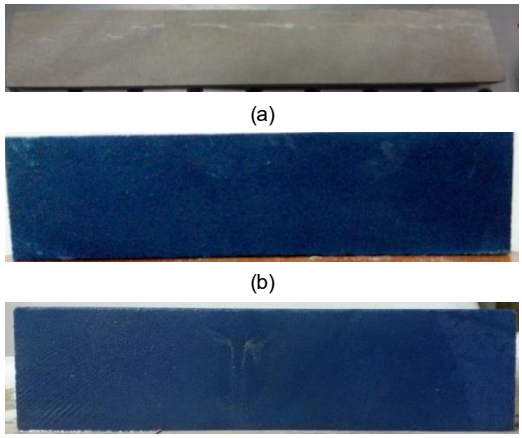

(a)

(b)

(c)

Figure 2 The prepared mortars used in the experiments (a) The unaffected graffiti (b) The dry blue-painted sample and (c) The wet blue-painted sample.

In this work, a Q-switch Nd:YAG laser operating at 1 Hz serves as the cleaning beam. The pulse duration of the laser is 10 ns. The laser provides the fundamental emission of 1064 nm. The laser fluence (energy density) of the laser cleaning beam can be varied using the Z-scan technique achieved by the scanning lens. The sample under investigation is then cleaned by the Z-scan laser beam. The efficiency of laser cleaning can be investigated through the optical setup. To be completeness, the laser removal of graffiti from mortars under dry and wet conditions was examined.

Results and Discussion

Figure 3 shows the cleaning results by varying Z positions with the fixed energy at 0.17 J.

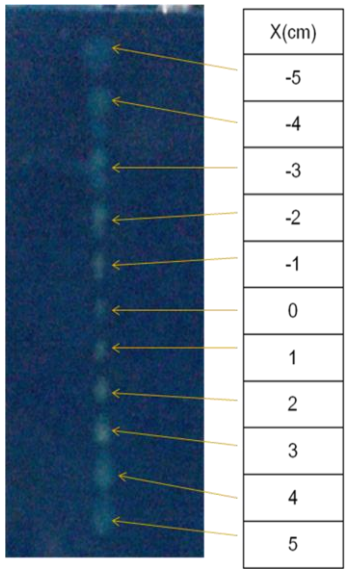

Figure 3 The laser cleans graffiti on mortars under varied z scanning.

The probe beams are detected by photodiodes. The level of signals obtained by these photodiodes can indicate to the satisfied cleaning situation.

Figure 4 shows the relation of unaffected graffiti signal and the laser treated signal under the dry condition.

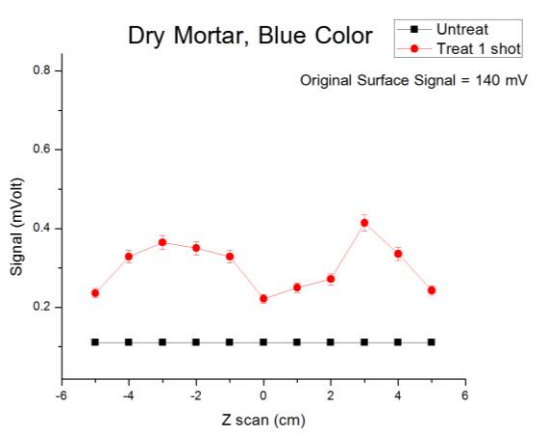

Figure 4 The relation of dry mortars at varied z-scanning.

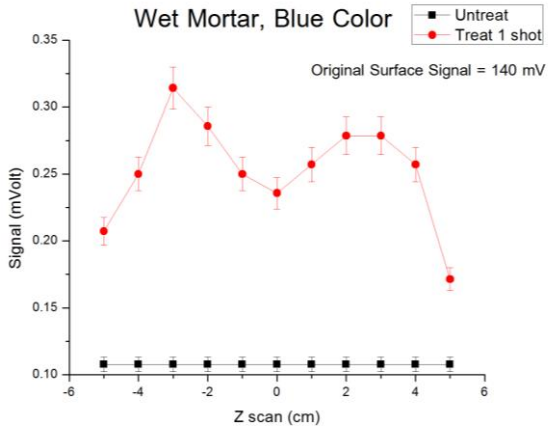

Figure 5 The relation of wet mortars at varied z-scanning

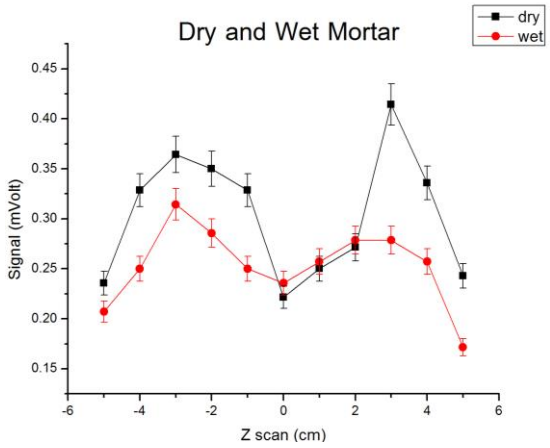

Figure 6 The relation of wet and dry mortars at varied z-scanning.

Figure 5 provides the signals obtained by the laser cleaning on the wet conditions. In addition, the results obtained by the laser cleaning on wet and dry mortars are shown in Figure 6. These signals are meant to determine the cleaning efficiency.

It is clearly that the cleaning threshold can be estimated by naked eyes. It is evident that the x=±3 cm of z-scanning is sufficient to remove the painted surface. It should be mentioned that the laser treatments were repeated for 50 times to ensure the obtained results.

Conclusions

The experiments were divided into two groups, the dry blue-painted and wet blue-pained samples. The cleaning threshold is x=±3 cm of Z-scanning setup. In trials, the laser cleaning has been demonstrated at removing the graffiti from the surface of the mortars. The cleaning samples were investigated by means of the Z-scan method during the cleaning procedures. The detected signals of the laser treated samples were compared under dry and wet conditions. This optical diagnostic setup can be further developed to assist laser cleaning technology thus providing interests in several applications.

Acknowledgments

This research work is financially supported by King Mongkut's University of Technology North Bangkok, Contact no. KMUTNB-GEN-57-26.

References

[1] Stephen, G. 2007. “Graffiti of Historic Surfaces”. **The Building Conservation Directory.**

[2] Lindsay, B. 2014. “Bombing, Tagging, Writing: An Analysis of the Significance of Graffiti and Street Art”. **Scholarly Commons.** University of Pennsylvania, Philadelphia, PA.

[3] Billy, H., Eleano,r B. and Kurt, I., 2013. “Spatio-temporal analysis of graffiti occurrence in an inner-city urban environment”. **Applied Geography.** (38): 53-63.

[4] Fiorucci, M.P., *et al.* 2012. “Optimization of graffiti removal on natural stone by means of high repetition rate UV laser”. **Applied Surface Science. (**278): 268–272.

[5] Yayun, Y., *et al.* 2014. “Laser cleaning of contamination on sandstone surfaces in Yungang Grottoes” **Optik**. (125): 3093–3097.

[6] Esbert, R.M. *et al.*, 2003. “Application limits of Q-switched Nd:YAG laser irradiation for stone cleaning based on colour measurements”. **Journal of Cultural Heritage.** 4 : 50s–55s.

[7] Penide, J., *et al.* 2013. “Removal of graffiti from quarry stone by high power diode laser”. **Optics and Lasers in Engineering**. (51): 364-370.

[8] Carmona, N., *et al.* 2011. “Laser cleaning of 19th century Congo rattan mats”. **Applied Surface Science**. (257): 9935-9940.

[9] Ortiz, P., *et al.* 2013. “Comparative study of pulsed laser cleaning applied to weatheredmarble surfaces”. **Applied Surface Science**. (283): 193-201.

[10] Kazimierz, R., *et al.* 2001. “Some experimental results of laser beam interaction with surface layer of brick”. **Building and Environment**. (36): 585-491.

[11] Sasha, C., 2000. “**Laser technology for graffiti removal**”. J. Cult. Heritage. (1): S75–S78.

[12] Phumipat, K., Jidapa, R., and Amarin, R. 2015. “An optical surface measurement for laser removal of graffiti”. **Proceeding of Siam Physics Congress**. pp. 4-7.

An Off-Axis Laser Recirculation

A Nisup*, S. Sirikunkitti, K. Chongcharoen and A. Ratanavis

Department of Industrial Physics and Medical Instrumentation, Faculty of Applied Science, Lasers and Optics Research Group (LANDOS), Science and Technology Institute. King Mongkut's University of Technology North Bangkok,Bangkok, Thailand

*E-mail: fig_phy.kmutnb@hotmail.com

Abstract

This paper presents a development of an optical arrangement that captures photons traveling in the multi-pass fashion based on a so-called laser recirculation. An optical trapping scheme is relied on the principle of nonlinear frequency conversion. In this demonstration, a L-shape resonator performing as the master cavity provides a laser beam with a fundamental frequency to create the frequency-doubled photon. The frequency-doubled laser beam is trapped inside the slave cavity which is designed to be an off-axis resonator. A retroreflector allows the off-axis configuration of the slave cavity. The alignment and trip of the photons was governed by lenses and mirrors of the slave cavity. To prove this novel concept, the demonstration is achieved by using a Quasi-CW pumped Nd:YAG laser at 1064 nm. In the master cavity, this fundamental frequency beam is incident on a nonlinear crystal (OPO) placed inside the cavity to generate the frequency-doubled laser beam at 532 nm. The frequency-double laser beam is then trapped inside the slave cavity. The retroreflector controls the trajectory of such a beam. A lens telescope is placed inside the slave cavity to collimate the laser beam. Using this off-axis laser recirculation, the interference problem can be alleviated. The optical setup is also insensitive to environmental vibration that allows to be operated in a hostile environment. Using an optical ray tracing program, the effective mode volume for the slave cavity can be calculated. The simulation can also predict the maximum roundtrips for various situations. The off-axis laser recirculation shows the promise of the simple robust and reliable multi-pass optical cavity which is suitable for laser spectroscopy and optical switching applications.

Keywords: Multi-pass laser cavity, Laser recirculation, Nonlinear optics

Introduction

Gas media shows great promises in laser spectroscopy in the sense of a great candidate for laser media emitting infrared light and friendly heat management. However, gas media suffer to their low absorption to commercial available light sources.

In the aspect of development of optically pumped molecular lasers (OPMLs), several optical configurations has been attempted to survive this major drawback. Multi-pass configurations have been proposed to gain higher absorption. It still remains as a challenge to invent multi-pass configuration for the gas laser excitation [1,2].

For the invention, the restriction of the law of reflection mainly prohibits desirable roundtrips. The zigzag optical pathways have been created to

accomplish multi-pass fashion. However the overlap of laser pathways play as an important role for the optical pumping schemes. This difficulty reveals the efficiency for the optical excitation. The pumping laser injecting from the external cavity reaches such a limitation. The exploration for the new optical configuration is meant to be continued.

In recent years, it has been several interests in the optical setup called laser recirculation [3-5]. A new frequency is created inside the multi-pass optical setup. In this configuration, the master cavity directs the pumping laser to excite a secondary medium. The excitation generates photons with different frequency that will be captured inside the slave cavity.

An optical system of laser recirculation was originally designed for experiments in Compton scattering. In addition the optical system of laser recirculation can be designed to obtain standing wave and traveling wave configurations. In an each round of the excitation, the excited laser is directed in the optical axis that provides the completely overlap beam resulting the high efficiency of the excitation [3-5].

However the laser recirculation reveals disadvantage on its sensitivity to vibration and arrangement. In addition the cost of optical setup is proportional to the specific optical arrangement.

In this paper we present an improvement in optical system of laser recirculation. An off-axis laser recirculation is proposed as an alternative multi-pass configuration.

An optical system off-axis laser recirculation benefits in the sense of the stability arrangement of the trapped beam. In addition, it should be clear that the interference of the trapped beam is very small. Therefore the off-axis laser recirculation can be used in the field and situations regardless to environment and unfavorable factors. Moreover, this invention can be used as a tool to study the radiation of matters such as solid, liquid, gas, plasma, etc.,

Materials and Methods

This optical setup comprises of two cavities which are called the master cavity and slave cavity. For the master cavity, it composes of a Quasi-CW pumped Nd:YAG laser at 1064 nm while the L-shape slave cavity using a nonlinear crystal (KTP) [6,7] placed inside the cavity to generate the frequency-doubled laser beam at 532 nm. In order to control the beam trajectory, a telescope system is placed inside the slave cavity. The retroreflector plays as a key to form the off-axis trajectory of such a beam [8]. As shown in Figure 1, the frequency-double laser beam is then trapped inside the slave cavity.

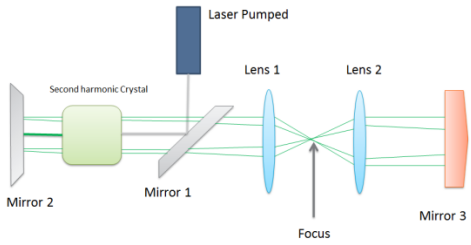

Figure 1 Schematic diagram of experiment. An off-axis laser recirculation by using a Quasi-CW pumped Nd:YAG laser at 1064 nm and a nonlinear crystal (KTP) placed inside the cavity to create the 532 nm photons.

Figure 1 also shows the useful position which is the focal points in the telescope. Such a position can be used to excite matters which are in the subject of spectroscopy study in the multi-pass approach.

Figure 2 Experiment setup of laser recirculation.

Figure 2 shows the setup of the off-axis laser recirculation. An Iodine vapor cell is placed at the focusing position to testify the ability of multi-pass excitation [9].

To estimate the capability of the off-axis laser recirculation, a ray tracing program is used. By varying angles of the initial trajectory, the obtainable roundtrips can be determined. Figure 3 shows the example of the simulation of the off-axis laser recirculation. According to the simulation, one unit cell means for one roundtrip [10].

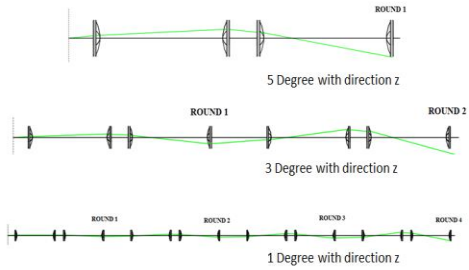

Figure 3 Example of the simulation calculated by a ray tracing program.

Results and Discussion

Figure 4 shows an example of results occurred by the off-axis laser recirculation. There are 8 dots shown on the retroreflector representing the total roundtrips of 4.

The roundtrips provided by the optical system are related by the alignment of the retroreflector. It should be noted that the maximum reachable roundtrip is 4 due to the optical losses in the slave cavity.

It is evident that the limitation of roundtrips reveals the consideration of the optical losses inside the slave cavity. To increase the number of roundtrips, the specific optical elements have to be designed for the wavelength of 532 nm.

To study the idealized design where the optical losses can be neglected, the ray tracing program can simulate the maximum achievable roundtrips. By varying the angle of the retroreflectior, the roundtrips can be determined.

Figure 5 shows the relation between the varying angles and the obtainable roundtrips. It should be noted that the angles measured are respected to the optical axis of the slave cavity. It is evident that the angle deflected of the optical axis plays as an important parameter to the number of roundtrips.

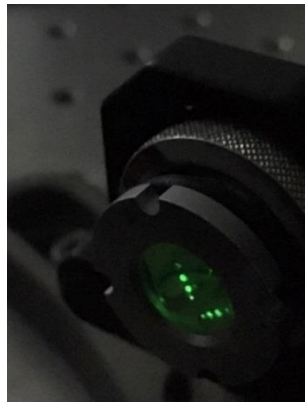

Figure 4 The number of dots represent the number of roundtrips. For this example, 8 dots indicates to 4 roundtrips.

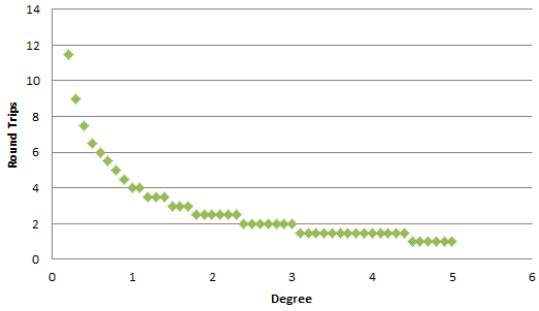

Figure 5 Comparison between varied angles and roundtrips.

It should be mentioned that the effective mode volume for the slave cavity can be calculated by using the information obtained by the simulations. It should be cleared that the effective mode volume is strongly relied on the varied angles of the beam.

Conclusions

In this study, an off-axis laser recirculation has been proposed as an alternative multi-pass laser cavity. The off-axis cavity provides the exceptional stability for multi-pass applications. The maximum roundtrips is 4 due to high optical loss in the slave cavity affected on the wavelength of 532 nm. Based on the simulation, the achievable roundtrips depends on the varied angle respected to the optical axis of the slave cavity. This off-axis laser recirculation can be further developed to serve as the multi-pass laser cavity, optical delays and multi-pass cells in applications on laser spectroscopy.

Acknowledgments

This research work is financially supported by King Mongkut's University of Technology North Bangkok (KMUTNB-GEN-56-22).

References

[1] Xu, B., et al. 2016. "Single-and multi-wavelength Nd:YAlO3 lasers at 1328, 1339 and 1364 nm". **Optics & Laser Technology**. 81: 1-6.

[2] Georges, P., et al. (1991). "High-efficiency multipass Ti:sapphire amplifiers for a continuous-wave single-mode laser." **Optics Letters**. 16 : 144–146.

[3] Jovanovic, I., Shverdin, M., Gibson, D., and Brown, C. 2011. "High-power laser pulse recirculation for inverse Compton scattering-produced gamma-rays". **Nuclear Instruments and Methods in Physics Research A**. 578: 160-171.

[4] Nilaya, J.P., and Biswas, D.J. (2015). "Exploitation of an external unstable multipass cavity to enhance the second harmonic conversion efficiency." **Optics Communications**. 341: 155-159.

[5] Rollason, A.J., Fang, X., and Dugdale, D.E. (2004). "Multipass optical cavity for inverse Compton interactions." **Nuclear Instruments and Methods in Physics Research A**. 526 : 560-571.

[6] Hu, J., and Hu, Z. (2009). "Growth and properties of KTP crystals from a new flux." **Crystal Growth**. 311 : 4235-4240.

[7] Saito, T., Honda, N., and Saito, H. (1999). "Advantage and disadvantage of KTP-532 laser tonsillectomy compared with conventional method." **Auris Nasus Larynx**. 26 : 447–452.

[8] Nagib, N.N. (2013). "Prism-type retroreflector of stable quarterwave retardance over extended spectral ranges." **Optics & Laser Technology**. 49: 47-50.

[9] Musha, M., et al. (2000). "The short- and long-term frequency stabilization of an injection-locked Nd:YAG laser in reference to a Fabry–Perotcavity and an iodine saturated absorption line." **Optics Communications**. 183: 165–173.

[10] Cai, Q., Xiangli, B., and Fang, Y. (2016). "Optical simulation of large aperture spatial heterodyne imaging spectrometer." **Optics Communications**. 366: 136-141.

Synthesis and Characterization of Titanium Nitride by RF Magnetron Sputtering

W. Nupangtha and D. Boonyawan*

Plasma and Beam Physics Research Facility, Department of Physics and Materials Science

Faculty of Science, Chiang Mai University, Chiang Mai, 50200, Thailand

*E-mail: porwasin@gmail.com

Abstract

This paper aim to find optimize deposition conditions of Titanium nitride thin film by change nitrogen feeding configuration and various sputtering parameters such as nitrogen flow rate, d-s (target-to-substrate distance) and power on structural and wettability of titanium nitride films deposited on glass substrate by RF magnetron sputtering. The proper plasma conditions used to deposit Titanium nitride film were carried out by the optical emission spectroscopy (OES). The film physical properties will be analyzed by contact angle.

Keywords: Titanium nitride (TiN), RF magnetron sputtering, Optical Emission Spectroscopy, Contact angle

Introduction

Titanium nitride (TiN) coatings using PVD (physical vapor deposition) techniques have been very successfully in a variety of applications because they exhibit a number of properties similar to metals such as goods 1electrical conductivity while retaining characteristics covalent bonds, hardness, and a high melting point found in insulating materials. Thin films can be sputtered by various procedures such as DC reactive sputtering and RF reactive sputtering [1]. However, we use RF sputtering process because the use of DC in plasma requires electrically conductive electrodes [2]. If one or both of the electrodes are non-conductive, e.g. when the glow discharge is used for the deposition of dielectric films, where the electrodes become gradually covered with insulating material, the insulator would charge up and terminate the discharge. The use of an alternative current AC power source can alleviate this problem because positive charges accumulated during one half-cycle can be neutralized by electron bombardment during the next cycle [3-6].

This research aims to study and develop the setup and procedure to find optimize deposition conditions of Titanium nitride thin film prepared by RF pulse reactive magnetron sputtering as shown in the drawing in Figure 1 using various sputtering parameters such as nitrogen flow rate, d-s (target-to-

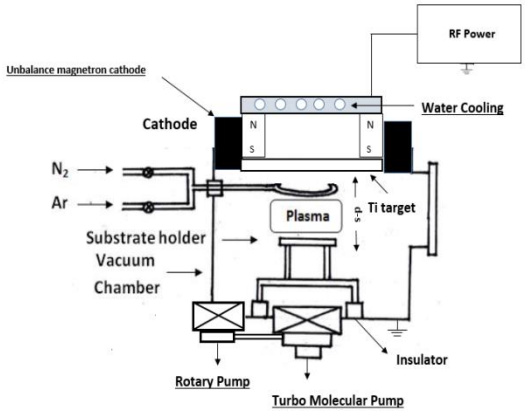

Figure 1 A schematic diagram of the experimental setup before separated nitrogen gas feeding.

sputtering parameters such as nitrogen flow rate, d-s (target-to-sputtering as shown in the drawing in Figure 1 using various sputtering parameters such as nitrogen flow rate, d-s (target-to-substrate distance) and power on structural. The wettability and physical properties of titanium nitride films deposited on glass substrate were investigated using contact angle.

Materials and Methods

A schematic diagram of the experimental setup with the optical spectroscopy (OES) system is shown in Figure 2. The sputtering chamber made of a stainless-steel, rectangular-shaped with 37 x 37 x 37 cm^3 in dimension. The cathodic target was a 99.999% pure Ti with a diameter of 100 mm. The target-to-substrate distance was vary from 3.5 to 8 cm. The system was evacuated by using a turbomolecular pump backed by rotary pump giving a base pressure less than 9 $x10^{-6}$ Torr. In this experiment, nitrogen gas was separated and fed through a distribution ring positioned below the argon gas feeding about 50 mm. The flow rates of each gas were controlled by using a MKS mass-flow controller.

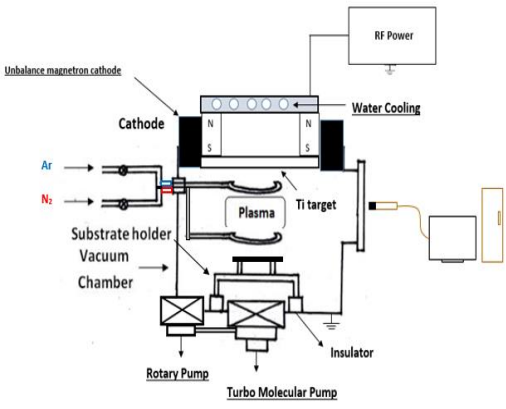

Figure 2 A schematic diagram of the experimental setup after separated nitrogen gas feeding

Argon (99.9995%) gas flow rate was fixed at 55 sccm. Nitrogen gas (99.9995%) flow rate was varied from 1, 3 and 6 sccm. The sputtering pressure was varied from 5 $x10^{-3}$ to 5 x 10^{-2} Torr. The sputtering power was varied from 100 to 200 watt. The frequencies of power source generally used for these alternating voltages are typically in the radiofrequency (RF) range (1 kHz–103 MHz; with a most common value of 13.56 MHz

Glass slide size 1 ×1 cm and 1.1 mm thick were clean by sputter surface of the substrate using argon ions for 5 min. To characterize the plasma conditions used to deposit TiN film RF reactive sputtering system. The plasma emission spectra from of deposited plasma were recorded through the UV quartz window on the side of the deposition chamber as shown in Figure 2. An optical emission spectrometer is AvaSpec 2048 Miniature Fiber Optic Spectrometer that can operate effectively with a full range fiber optic and analyze with AvaSoft program. The optical emission spectra were recorded in the wavelength range 200 to 800 nm.

Synthesis of titanium nitride film, glass slides size 1 ×1 cm were sputtered at different plasma conditions by varying nitrogen gas feeding at 1-9 sccm, RF power operate at 100-200 watt and d-s (target-to-substrate distance) at 3.5 - 8 cm and time 60 minute. After that, analysis “hydrophobic” or “hydrophilic” properties of titanium nitride film by contact angle technique. That we used micropipette to drop the DI water of 15 μl on the surface of glass slide sample.

Results and Discussion

The OES spectra of Ar-N2-Ti (Figure3) and Ti (Figure 4) were observed in the range of 200 – 800 nm wavelength. The identification of atoms and diatomic molecules was carried out with the aid of the

NIST Atomic Spectra Database. In the spectrum of the deposited plasma compare between before (blue line) and after (red line) separate nitrogen gas feeding (Figure 3) spectral lines and bands of N_2 (337.1), Ti (451) and Ar (696.5) were identified.

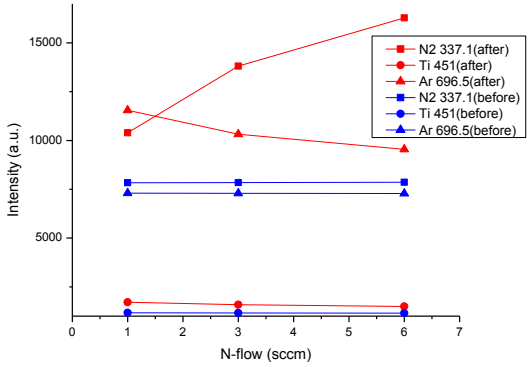

Figure 3 The OES spectra of Ar-N_2-Ti comparative.

The emission intensities of the analyzed atomic lines and molecular bands were investigated. It can be seen from Figure 3 when separated the nitrogen gas feeding, the N_2 (337.1), Ti (451) and Ar (696.5) peaks intensity (red line) increase more than peak intensity before change nitrogen gas feeding (Blue line) due to highly concentration of argon gas around target zone.

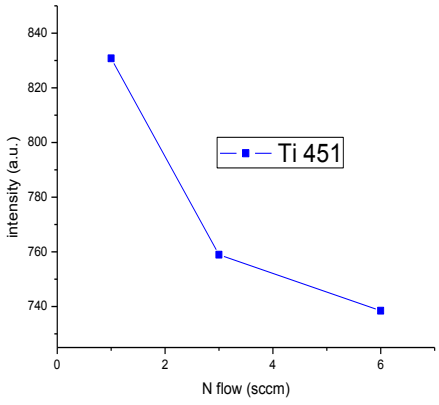

Figure 4 The OES spectra of Ti (451) at different N_2 flow rate.

From Figure 4, The Ti (451) peak intensities decrease with increasing the N_2 content (1, 3 and 6 sccm) the maximum intensity spectra of Ti (451) appear in at 1 sccm of nitrogen gas feeding.

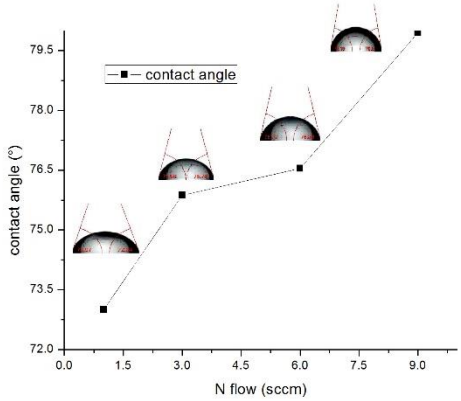

Figure 5 Contact angles of test liquids on the coatings at P= 200 watt and N_2 flow from 1 to 9 sccm.

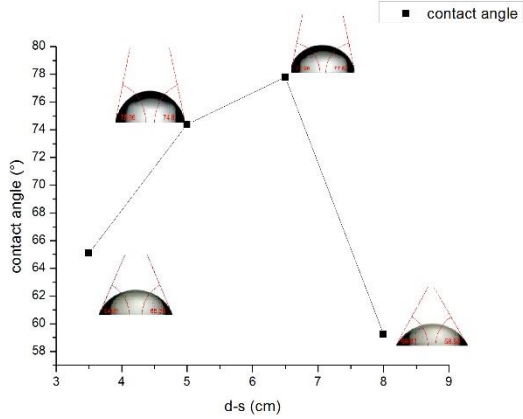

Figure 6 Contact angles of test liquids on the coatings at P= 200 watt, N_2 flow=1sccm and d-s from 3.5 to 8 cm.

Figure 5 shows the contact angles at N_2 flow from 1 to 9 sccm. The contact angle increase with increasing nitrogen flow rate. The lowest contact angle appears in the film formed at 1 sccm. In the Figure 6 show the contact angles at d-s from 3.5 to 8 cm. when increase d-s (target-to-substrate distance), the

proper sputtering conditions for the deposition TiN appears in the film formed at 8 cm about 58.1 deg, as shown in Figure 7.

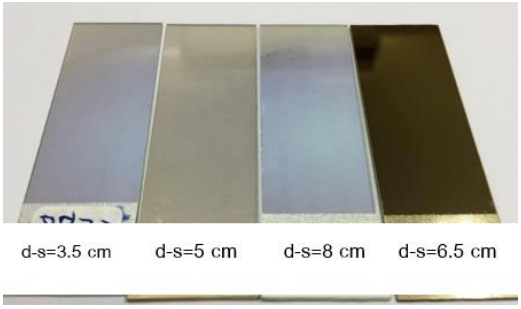

Figure 7 Surface characteristics and colors of TiN thin films deposited on glass slide under various d-s (target-to-substrate distance).

According to Young's equation, there is a relationship between the surface free energy γ_{SV} of the solid, the contact angle θ, the surface tension of the liquid γ_{SL} and the interfacial tension γ_{LV} between liquid and solid:

$$\gamma_{SV} = \gamma_S + \gamma_{LV} cos\theta_c \quad (1)$$

$$W_a = \gamma_{LV}(1 + cos\theta_c) \quad (2)$$

where the energy of adhesion (W_a) is directly related to the surface free energy of the contact between two phases. Therefore, lower adhesion (anti-adhesion) corresponds to lower surface free energy. Deionized water that has a higher surface tension (72.8 millinewtons per meter at 20 °C) was used to measure work of adhesion. The work of adhesion of contact angle at 58.1, 65.1, 75.33 and 77.79 deg. is 111.27, 103.45, 91.24, 88.19 dynes/cm respectively, so the highest work of adhesion of titanium nitride as-deposited film is 111.27 dynes/cm.

Table 1 Surface energies of titanium nitride films deposited at N_2 flow 1sccm and d-s in range 3.5-8 cm

Substrates	d-s (cm)	Contact angle (θ)	Work of adhesion W_a (dynes/cm)
This study	3.5	65.1	103.45
	5	75.33	92.14
	6.5	77.79	88.19
	8	58.1	111.27
TiN [3]		44.3	124
TiN [4]		60.5	108.65

Conclusions

From the results, the emission intensity of deposited plasma investigated by OES after separate nitrogen gas feeding, the optimize deposition conditions of Titanium nitride thin film is power 200 watt, N_2 flow 1 sccm , d-s 8 cm and deposition time 60 minutes. In addition, the contact angle of titanium nitride as-depostited film is hydrophilic with with rf power 200 w, N_2 flow 1 sccm and (d-s) 8 cm. the work of adhesion is 111.27 dynes/cm.

Acknowledgments

This work has been supported by the CMU Junior Research Fellowship Program, Plasma and Beam Physics Research Facility, Department of Physics and Materials Science, Faculty of Science, Chiang Mai University, and the Science Achievement Scholarship of Thailand (SAST). The authors would like to acknowledge the financial support to participate this

conference by the Faculty of Science, Chiang Mai University.

References

[1] Wongpisan W., et al. (2013). *Chiang Mai J. Sci., 40(5),*857-864.

[2] Boonyawan D. Characterization of titanium nitride-hydroxyapatite on PEEK for dental implants by co-axis target magnetron sputtering. *Chiang Mai University*

[3] Mezger P.R. and Creugers N.H. (1992). Titanium nitride coatings in clinical dentistry**.** *J Dent., 20(6),* 342-4.

[4] Al Jabbari Y.S., et al. (2012). Titanium Nitride and Nitrogen Ion Implanted Coated Dental Materials. *Coatings., 2(3)*, 160-78.

[5] Tian X.B., et al. (2002). Influence of bias voltage on the tribological properties of titanium nitride films fabricated by dynamic plasma ion implant-ation/deposition. *Surf Coat Technol., 161(2),* 232-36.

[6] Vadiraj A. and Kamaraj M. (2006). Fretting fatigue studies of titanium nitride-coated biomedical titanium alloys, *J. Mater. Eng. Perform., 15*, 553–557.